LS Scienza dei Materiali - a.a. 2006/07

Fisica delle Nanotecnologie – part 6

Version 5, Dec 2006

Francesco Fuso, tel 0502214305, 0502214293 - fuso@df.unipi.it
http://www.df.unipi.it/~fuso/dida

Nanotecnologie in ottica e fotonica: emissione da sistemi confinati e laser, quantum dots, plasmoni, cristalli fotonici

1/12/2006 – 14.30-16.30 – room T1

Introduction to the topic

Optics (in the visible, $\lambda \approx 400–700$ nm)
vs nanotechnology (dimensions typ. < 100 nm)
***Different dimensional scales*!!**

But:

-Semiconductive nanostructures (e.g., MQW, QD) are essential for providing peculiar optical features exploited, for instance, in diode lasers

- Nanosized metal structures exhibit peculiar optical response (e.g., plasmon resonances)

- Nanostructured materials can "manipulate" radiation (e.g., photonic band gaps, *near-field optics (as we have already seen!)*

Great (and partially new) interest is stemming on optics and nanosized structures

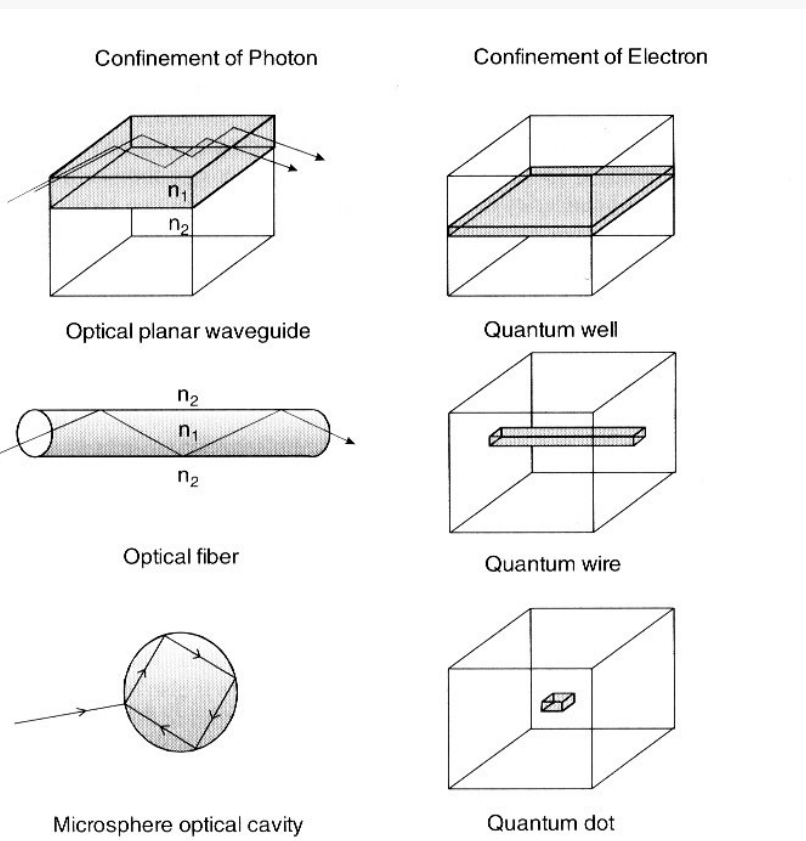

Figure 2.2. Confinements of photons and electrons in various dimensions and the configurations used for them. The propagation direction is *z*.

Da P.N. Prasad,
Nanophotonics,
Wiley (2004)

Outlook

- Only inorganic materials will be treated (emission in organics to be discussed later on!)
- Issues relevant for near-field optics have been already treated

Major issues

1. "Conventional" (heterostructure) diode lasers vs "nanotechnological" lasers (e.g., DBR, QD, VCSEL, ...) exploiting **quantum confinement** in semiconductors (electroluminescence)
2. Quantum dots and nanocrystals for photoluminescence applications
3. Metallic nanostructures (nanoparticles) and a few words on plasmon resonances
4. A few words on manipulation and confinement of radiation in structured samples (e.g., photonic crystals)

1. How to build a diode laser (or a LED)

Broad diffusion of lasers driven by the availability of solid-state active media, but (bulk) semiconductors, e.g., Si, are not suited because of energy gap (in the IR) and indirect transitions

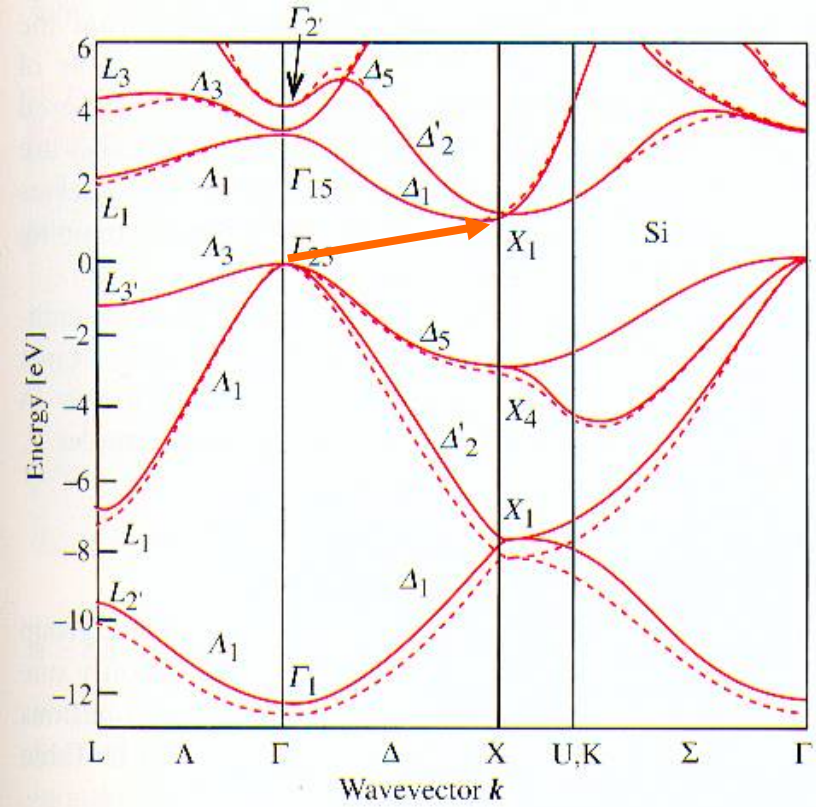

Fig. 2.10. Electronic band structure of Si calculated by the pseudopotential technique. The *solid* and the *doted lines* represent calculations with a **nonlocal** and a **local pseudopotential**, respectively. [Ref. 2.6, p. 81]

Band structure of Si

The top of valence band and the bottom of the conduction band are displaced each other

⇩

Momentum conservation implies phonons to be involved in the absorption process

⇩

Transition probability is small (10^{-5}-10^{-6} s^{-1}) (and wavelength is in the IR, above 1 μm)

Bulk semiconductive materials can be hardly used in optoelectronics devices

Da Yu and Cardona
Fundamentals of Semicond.
Springer (1996)

Semiconductive heterostructures

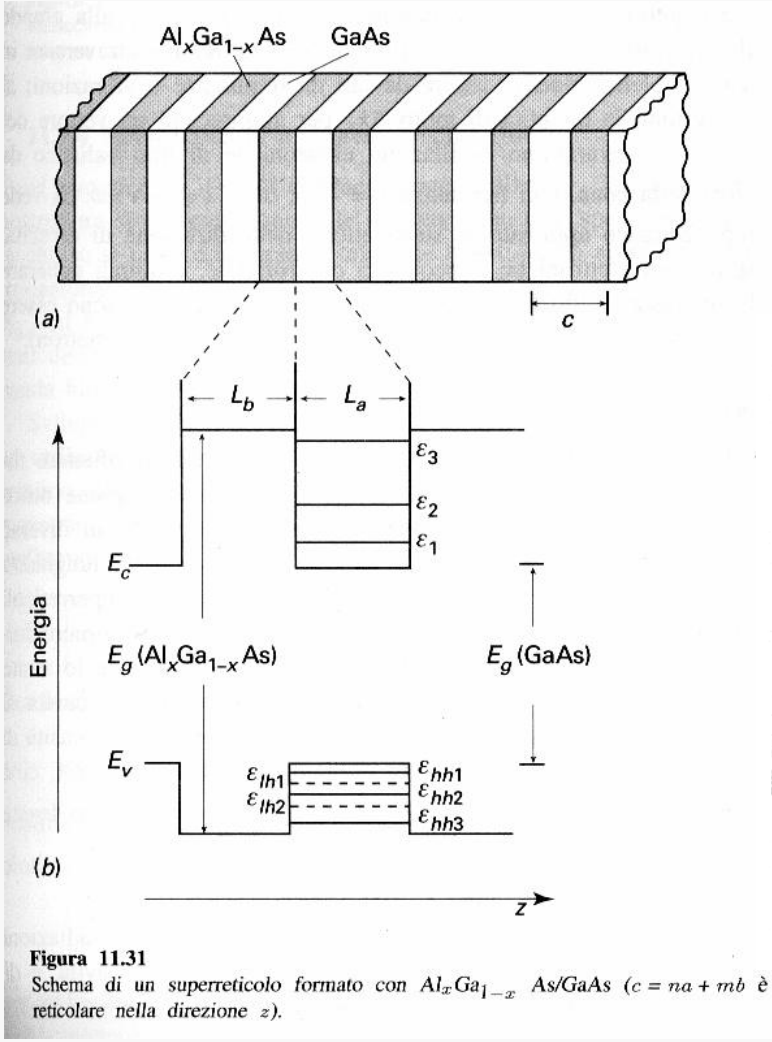

Figura 11.31
Schema di un superreticolo formato con Al_xGa_{1-x} As/GaAs ($c = na + mb$ è il parametro reticolare nella direzione z).

Heterostructures(superlattices): sequence of layers made of semiconductors with different gap energies (*as we have already seen!)*

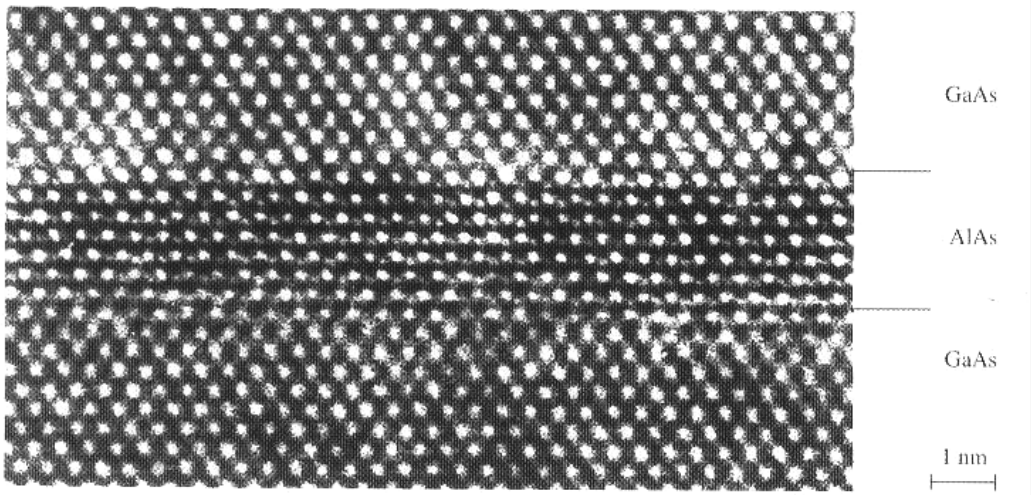

Fig. 9.1. High resolution transmission electron micrograph (TEM) showing a GaAs/AlAs superlattice for a [110] incident beam. (Courtesy of K. Ploog, Paul Drude Institute, Berlin.) In spite of the almost perfect interfaces, try to identify possible Al atoms in Ga sites and vice versa

Heterostructure growth through MBE
--> Lattice matching (pseudomorphism)
--> strain/stress
--> critical thickness (and dislocation)

Da Bassani Grassano,
Fisica dello Stato Solido,
Boringhieri (2000)

Quantum Well I

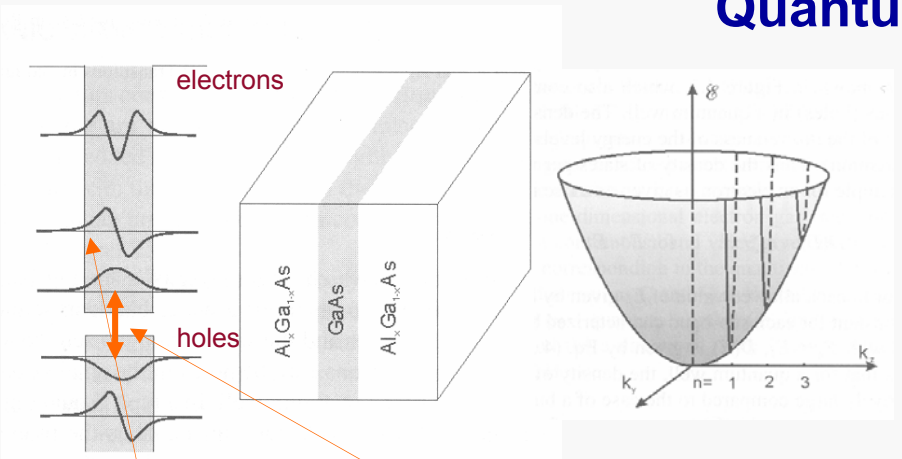

- For energies $E < V$, the energy levels of the electron are quantized for the direction z of the confinement; hence they are given by the model of particle in a one-dimensional box. The electronic energies in the other two dimensions (x and y) are not discrete and are given by the effective mass approximation discussed in Chapter 2. Therefore, for $E < V$, the energy of an electron in the conduction band is given as

$$E_{n,k_x,k_y} = E_C + \frac{n^2h^2}{8m_e^* l^2} + \frac{\hbar^2(k_x^2 + k_y^2)}{2m_e^*} \qquad (4.1)$$

where $n = 1, 2, 3$ are the quantaum numbers. The second term on the right-hand side represents the quantized energy; the third term gives the kinetic energy of the electron in the x–y plane in which it is relativelv free to move. The symbols used are as follows: m_e^* is the effective mass of electron, and E_C is the energy corresponding to the bottom of the conduction band.

Equation (4.1) shows that for each quantum number n, the values of wavevector components k_x and k_y form a two-dimensional band structure. However, the wavevector k_z along the confinement direction z takes on only discrete values, $k_z = n\pi/l$. Each of the bands for a specific value of n is called a sub-band. Thus n becomes a sub-band index. Figure 4.2 shows a two-dimensional plot of these sub-bands.

- For $E > V$, the energy levels of the electron are not quantized even along the z direction. Figure 4.1 shows that for the AlGaAs/GaAs quantum well, the quantized levels $n = 1$–3 exist, beyond which the electronic energy level is a continuum. The total number of discrete levels is determined by the width l of the well and the barrier height V.

- The holes behave in analogous way, except their quantized energy is inverted and the effective mass of a hole is different. Figure 4.1 also shows that for the holes, two quantized states with quantum numbers $n = 1$ and 2 exist for this particular quantum well (determined by the composition of AlGaAs and the width of the well). In the case of the GaAs system, two types of holes exist, determined by the curvature (second derivative) of the band structure. The one with a smaller effective mass is called a *light hole* (lh), and the other with a heavier effective mass is called a *heavy hole* (hh). Thus the $n = 1$ and $n = 2$ quantum states actually are each split in two, one corresponding to lh and the other to hh.
- Because of the finite value of the potential barrier ($V \neq \infty$), the wavefunctions, as shown for levels $n = 1$, 2, and 3 in the case of electrons and levels $n = 1$ and 2 in the case of holes, do not go to zero at the boundaries. They extend into the region of the wider bandgap semiconductor, decaying exponentially into this region. This electron leakage behavior has already been discussed in Section 2.1.3 of Chapter 2.
- The lowest-energy band-to-band optical transition (called the interband transition) is no longer at E_g, the energy gap of the smaller bandgap semiconductor, GaAs in this case. It is at a higher energy corresponding to the difference between the lowest energy state ($n = 1$) of the electrons in the conduction band and the corresponding state of the holes in the valence band. The effective bandgap for a quantum well is defined as

$$E_g^{\text{eff}} = (E_C - E_V) + \frac{h^2}{8l^2}\left(\frac{1}{m_e^*} + \frac{1}{m_h^*}\right) \qquad (4.2)$$

In addition, there is an excitonic transition below the band-to-band transition. These transitions are modifications of the corresponding transitions found for a bulk semiconductor. In addition to the interband transitions, new transitions between the different sub-bands (corresponding to different n values) within the conduction band can occur. These new transitions, called intraband or inter-sub-band transitions, find important technologic applications such as in quantum cascade lasers. The optical transitions in quantum-confined structures are further discussed in the next section.

Da P.N. Prasad,
Nanophotonics,
Wiley (2004)

Confinement of holes

Da Yu and Cardona
Fundamentals of Semicond.
Springer (1996)

b) Confinement of Holes in Quantum Wells

As we showed in Sect. 4.2.4, the equation of motion of holes in diamond- and zinc-blende-type semiconductors under the influence of a Coulomb potential is rather complicated even within the effective mass approximation. In the case of shallow acceptors discussed in that section, the solutions are simplified by the spherical symmetry of the potential. Since the QW confinement potential $V(z)$ is not spherical we expect the problem to be more difficult. Indeed numerical calculations are necessary to obtain meaningful results. An example of hole subbands obtained by such calculations is shown by the solid curves in Fig. 9.6 for a $GaAs/Ga_{0.7}Al_{0.3}As$ QW with well widths of 100 and 150 Å [9.18]. The labeling of the bands suggests that they arise from either the heavy hole (HH) or light hole (LH) bands of the bulk. We shall see that, strictly speaking, this is not the case since the bulk valence bands are heavily mixed by $V(z)$. These subbands can be qualitatively understood in the following way.

Let us assume that the spin–orbit splitting of the hole bands is so large that only the $J = 3/2$ heavy ($J_z = 3/2$) and light ($J_z = 1/2$) hole bands need be considered. Furthermore, the axis of quantization for J is chosen to be along the growth direction. Their dispersions in the bulk crystal can be calculated from the Luttinger Hamiltonian $\mathcal{H}_L$ in (2.70), to which the confinement potential $V(z)$ must be added. As we saw in Sect. 4.2.4, the cubic term, proportional to $(\gamma_3 - \gamma_2)$, is small in most zinc-blende-type semiconductors. For simplicity we neglect this term and further assume that the Luttinger parameters are identical in the layers A and B. With these simplifications, the hole Hamiltonian in a QW becomes

$$\mathcal{H}_{QW} = \left(\frac{\hbar^2}{2m}\right)\left[\left(\gamma_1 + \frac{5\gamma_2}{2}\right)\nabla^2 - 2\gamma_2\left(J_x\frac{\partial}{\partial x} + J_y\frac{\partial}{\partial y} + J_z\frac{\partial}{\partial z}\right)^2\right] + V(z). \quad (9.14)$$

The Schrödinger equation corresponding to this Hamiltonian is not separable because of the terms $J_xJ_y(\partial/\partial x)(\partial/\partial z)$ etc. obtained on expanding $(\boldsymbol{J}\cdot\nabla)^2$. Let us make the *ad hoc* assumption that the "off-diagonal" terms containing $(\partial/\partial x)(\partial/\partial z)$ etc. are small enough that they can be neglected at first and introduced later as perturbations (this should certainly be valid for small k_x and k_y). With this assumption the Schrödinger equation becomes separable into two equations as in (9.6). The Hamiltonian for motion in the z direction becomes

$$\left(\frac{\hbar^2}{2m}\right)\left[\left(\gamma_1 + \frac{5\gamma_2}{2}\right) - 2\gamma_2 J_z^2\right]\left(\frac{\partial}{\partial z}\right)^2 + V(z) \quad (9.15a)$$

This equation suggests that the $J_z = 3/2$ state (we shall avoid using the labels "heavy" and "light" because they are no longer meaningful as we shall see later) behaves, for the purpose of calculating the confinement properties with the Hamiltonian in (9.15a), as if its effective mass m_{hz} were equal to [cf. (2.67)]

$$(m_{hz})^{-1} = (\gamma_1 - 2\gamma_2)/m, \quad (9.16a)$$

while the $J_z = 1/2$ state acts as if it had the lighter mass m_{lz}

$$(m_{lz})^{-1} = (\gamma_1 + 2\gamma_2)/m. \quad (9.16b)$$

Since the confinement energy is inversely proportional to the effective mass, see (9.12), it is larger for the $J_z = 1/2$ state than for the heavy $J_z = 3/2$ state. This situation is shown schematically in Fig. 9.7a.

Numerical calculations

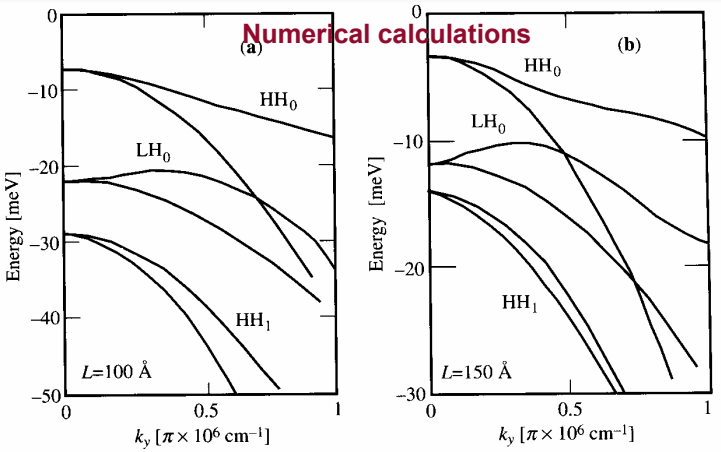

Fig. 9.6. Hole subband energies in a $GaAs/Ga_{0.7}Al_{0.3}As$ QW calculated by *Bastard* and *Brum* [9.18] within the envelope-function approximation for well widths of (**a**) 100 and (**b**) 150 Å, respectively. The labels HH and LH denote the subbands arising from the heavy and light hole valence bands in the bulk, respectively (*red curves*). The *black curves* represent the subband energies calculated when the mixing between the heavy and light hole bands is neglected

In zinc-blende type crystals (as most QWs) **hole** energy diagrams show a splitting (degeneracy is removed due to spin-orbit coupling)

"Light" and "Heavy" Holes states appear

Dimensionality and density of states (DOS)

Quantum confinement effects expected whenever boundary conditions are imposed by the size of the system

DOS and dimensionality

$$g(p)\,dp \propto \begin{cases} L/h\,dp & \text{1-D} \\ S/h^2\,2\pi p\,dp & \text{2-D} \\ V/h^3\,4\pi p^2\,dp & \text{3-D} \end{cases}$$

$$g(E)\,dE \propto \begin{cases} dE/\sqrt{E} & \text{1-D} \\ dE & \text{2-D} \\ \sqrt{E}\,dE & \text{3-D} \end{cases}$$

DOS expression affected by dimensions

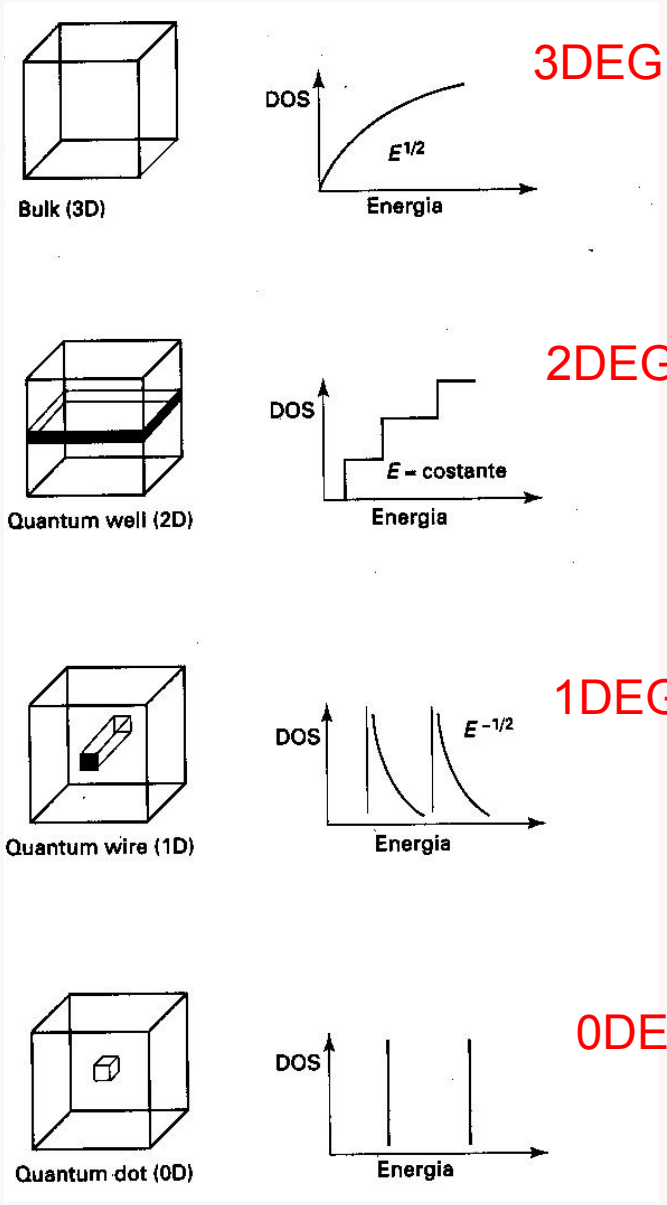

Quantum Well II

- Another major modification, introduced by quantum confinement, is in the density of states. The density of states $D(E)$, defined by the number of energy states between energy E and $E + dE$, is determined by the derivative $dn(E)/dE$. For a bulk semiconductor, the density of states $D(E)$ is given by $E^{1/2}$. For electrons in a bulk semiconductor, $D(E)$ is zero at the bottom of the conduction band and increases as the energy of the electron in the conduction band increases. A similar behavior is exhibited by the hole, for which the energy dispersion (valence band) is inverted. Hence, as the energy is moved below the valence band maximum, the hole density of states increases as $E^{1/2}$. This behavior is shown in Figure 4.3, which also compares the density of states for electrons (holes) in a quantum well. The density of states is a step function because of the discreteness of the energy levels along the z direction (confinement direction). Thus the density of states per unit volume for each sub-band, for example for an electron, is given as a rise in steps of

$$D(E) = m_e^*/\pi^2 \qquad \text{for } E > E_1 \tag{4.3}$$

The steps in $D(E)$ occur at each allowed value of E_n given by Equation (4.1), for k_x and $k_y = 0$, then stay constant for each sub-band characterized by a specific n (or k_z). For the first sub-band with $E_n = E_1$, $D(E)$ is given by Eq. (4.3). This step-like behavior of $D(E)$ implies that for a quantum well, the density of states in the vicinity of the bandgap is relatively large compared to the case of a bulk semiconductor for which $D(E)$ vanishes. As is discussed below, a major manifestation of this modification of the density of states is in the strength of optical transition. A major factor in the expression for the strength of optical transition (often defined as the oscillator strength) is the density of states. Hence, the oscillator strength in the vicinity of the bandgap is considerably enhanced for a quantum well compared to a bulk semiconductor. This enhanced oscillator strength is particularly important in obtaining laser action in quantum wells, as discussed in Section 4.4.

DOS

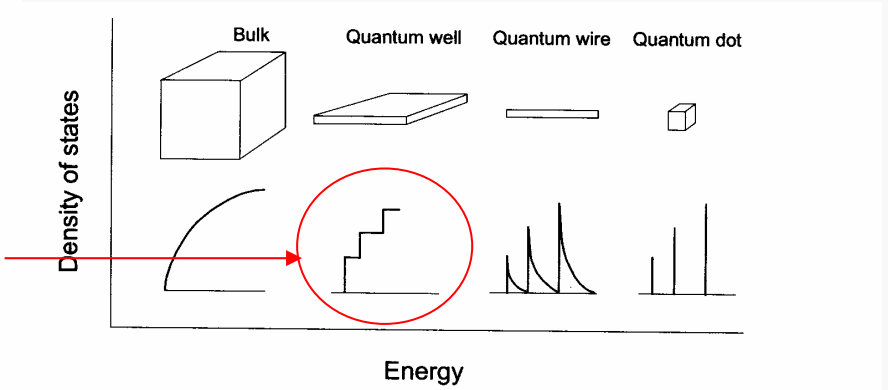

Figure 4.3. Density of states for electrons in bulk conduction band together with those in various confined geometries.

Optical transitions in quantum confined systems

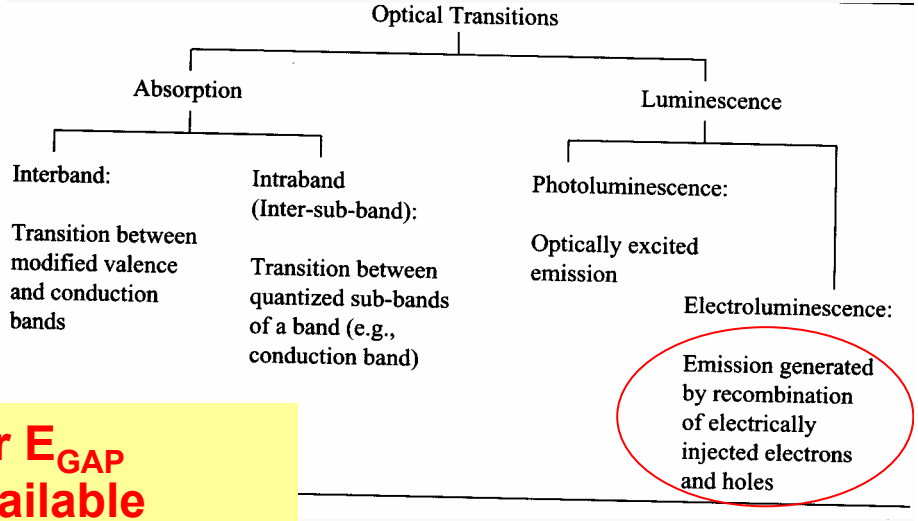

✓Interband transition energy is no longer E_{GAP}
✓Intraband (intersubband) transitions available
✓Increased transition "strength" (oscillator strength)

Excitons (a few words)

Whenever electron and hole wavefunctions overlap each other, a quasi-bound system can be formed called **exciton**

In (type I) quantum wells there is a high probability of exciton formation due to confinement of electrons and holes in the same layer

Il calcolo dell'energia di legame degli eccitoni può essere effettuato in modo analogo a quello delle impurezze nei semiconduttori se le bande di valenza e di conduzione sono sferiche e non degeneri. Analogamente a quanto visto nel cap. 11, si ricava che i livelli idrogenoidi (riferiti alla cima della banda di valenza) hanno energie date da:

Hydrogen-like energy levels!

$$E_n = E_g - \frac{\mu e^4}{2\hbar^2 \varepsilon^2} \frac{1}{n^2}, \qquad (12.107)$$

ove n è il numero quantico principale, ε la costante dielettrica, e μ la massa ridotta del complesso elettrone-buca

$$\frac{1}{\mu} = \frac{1}{m_e^\star} + \frac{1}{m_h^\star} \cdot \qquad (12.108)$$

Nei semiconduttori abbiamo visto che $\varepsilon \simeq 10$ e $\mu \simeq 0.5 m_e$, per cui l'energia di legame degli eccitoni sarà dell'ordine di qualche decina di meV. A causa della grande costante dielettrica l'eccitone è dunque debolmente legato e la distanza media elettrone-buca è dell'ordine di decine di distanze reticolari. Un eccitone con queste caratteristiche è chiamato eccitone di Wannier-Mott, e ne discuteremo

Electron and hole system bound by Coulomb forces

⇩

Exciton behaves like an hydrogen atom (but for some degeneracy removal, e.g., light and heavy hole states)

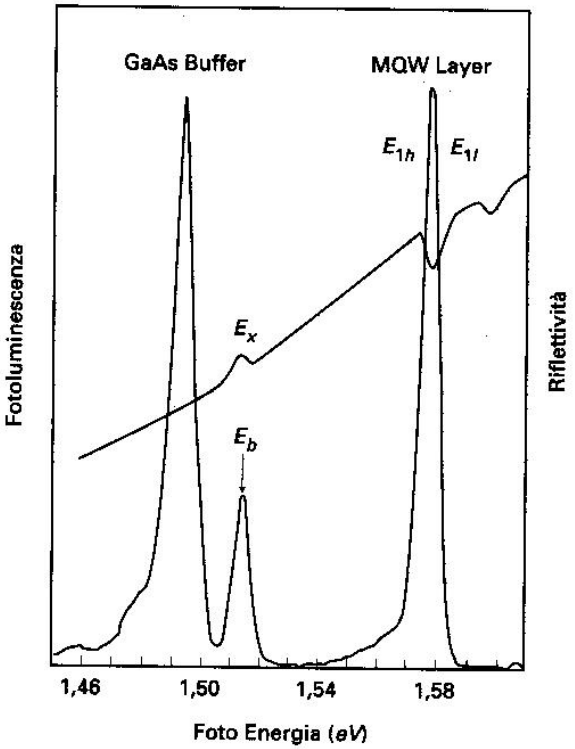

Figura 12.28
Fluorescenza eccitonica da un pozzo quantico (Q.W.) GaAs/$Ga_{1-x}Al_xAs$ e dal substrato GaAs a 12 K. E_b indica la posizione dell'eccitone nel substrato, E_{1h} ed E_{1l} gli eccitoni di buca pesante e di buca leggera nel Q.W. Per confronto è riportata anche la riflettività. Il picco di buca leggera compare soltanto ad alte temperature in fluorescenza, mentre è visibile in riflettività. (Da Y. Chen, R. Cingolani, L.C. Andreani, F. Bassani e J. Massies, Il Nuovo Cimento **D10**, 847 (1988)).

A superlattice is formed by a periodic array of quantum structures (quantum wells, quantum wires, and quantum dots). An example of such a superlattice is a multiple quantum well, produced by growth of alternate layers of a wider bandgap (e.g., AlGaAs) and a narrower bandgap (GaAs) semiconductors in the growth (confinement) direction. This type of multiple quantum wells is shown in Figure 4.10a,b by a schematic of their spatial arrangement as well as by a periodic variation of their conduction and valence band edges.

When these quantum wells are widely separated so that the wavefunctions of the electrons and the holes remain confined within individual wells, they can be treated as a set of isolated quantum wells. In this case, the electrons (or the holes) can not tunnel from one well to another. The energies and wavefunctions of electrons (and holes) in each well remain unchanged even in the multiple quantum well arrangement. However, such noninteracting multiple quantum wells (or simply labeled multiple quantum wells) are often utilized to enhance an optical signal (absorption or emission) obtainable from a single well. An example is lasing, to be discussed in the next section, where the stimulated emission is amplified by traversing through multiple quantum wells, each well acting as an independent medium.

To understand the interaction among the quantum wells, one can use a perturbation theory approach similar to treating identical interacting particles with degenerate energy states. As an example, let us take two quantum wells separated by a large distance. At this large separation, each well has a set of quantized levels E_n labeled by quantum numbers $n = 1, 2, \ldots$ along the confinement direction (growth direction). As the two wells are brought close together so that the interaction between them becomes possible, the same energy states E_n of the two wells are no longer degenerate. Two new states E_n^+ and E_n^- result from the symmetric (positive) overlap and antisymmetric (negative) overlap of the wavefunctions of the well. The $E_n^+ = E_n + \Delta_n$ and $E_n^- = E_n - \Delta_n$ are split by twice the interaction parameter Δ_n for level n.

The magnitude of the splitting, $2\Delta_n$, is dependent on the level E_n. It is larger for higher energy levels because the higher the value of n (the higher the energy value E_n), the more the wavefunction extends in the energy barrier region allowing more interaction between the wells.

The case of two wells now can be generalized into the case of N wells. Their interactions lift the energy degeneracy to produce splitting into N levels, which are closely spaced to form a band, the so-called miniband. In an infinite multiple quantum well limit, the width of such a miniband is $4\Delta_n$, where Δ_n is the interaction between two neighboring wells for the level n. This result is shown in Figure 4.11 for the two levels E_1 and E_2 for the case of a superlattice consisting of alternate layers of GaAs (well) and $Al_{0.11}Ga_{0.89}As$ (barrier), each of width 9 nm. For this system, the miniband energies are $E_1 = 26.6$ meV and $E_2 = 87$ meV, with the respective bandwidth of $\Delta E_1 = 2.3$ meV and $\Delta E_2 = 20.2$ meV (Barnham and Vvedensky, 2001). As explained above, the higher-energy miniband (E_2) has a greater bandwidth (ΔE_2) than the lower energy miniband (ΔE_1).

Multiple Quantum Wells

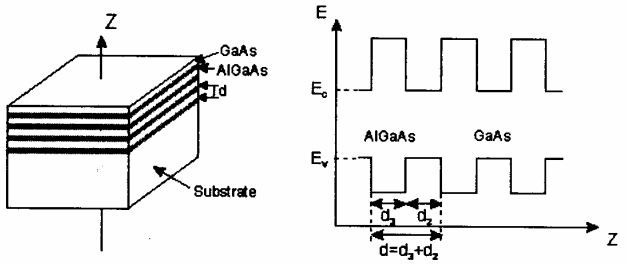

Figure 4.10. Schematics of the arrangement (a) and the energy bands (b) of multiple quantum wells.

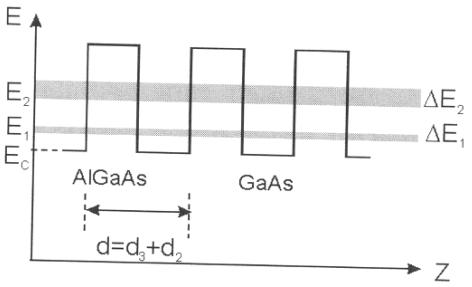

Figure 4.11. Schematics of formation of minibands in a superlattice consisting of alternate layers of GaAs (well) and AlGaAs (barrier).

✓"Minibands" formed due to interaction of different wells
✓Consequences in QC lasers *(see later on!)*

Kinds of MQW

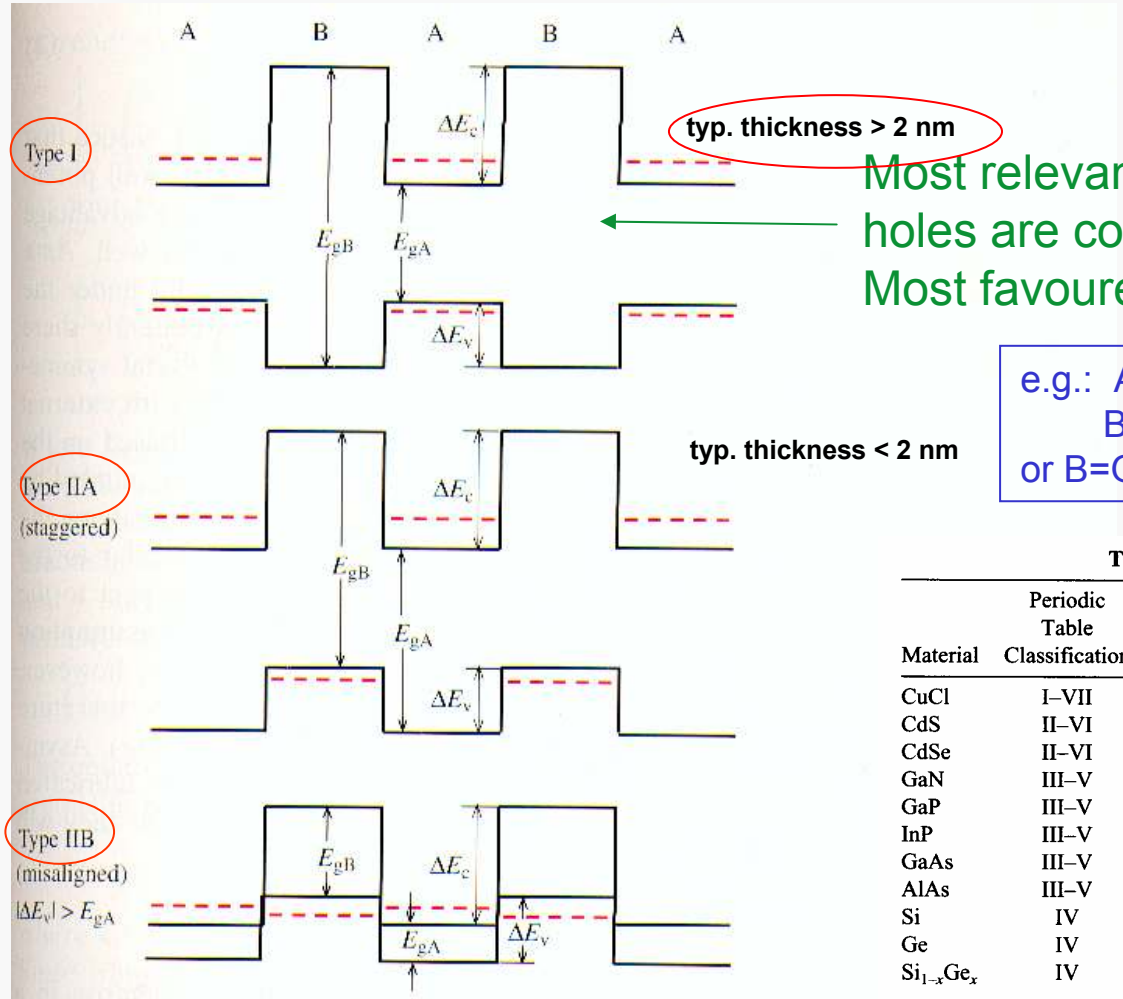

Fig. 9.3. Schematic diagrams of three arrangements of the confinement holes in MQWs and superlattices formed by two semiconductors A and E_{gA} and E_{gB}, respectively. In type I samples both the electrons and holes are confined in the same layer A. The energies of the confined particles are represented by *red lines*. In type IIA systems the electrons and holes are confined in different layers. Type IIB samples are a special case of type IIA behavior. They are either small gap semiconductors or semimetals

typ. thickness > 2 nm

Most relevant configuration: electrons and holes are confined in the same layer
Most favoured for exciton formation

typ. thickness < 2 nm

e.g.: A=GaAs (E_{gA} ~ 1.4 eV, lattice 5.653 Å)
B=AlAs (E_{gB} ~ 2.2 eV, lattice 5.62 Å)
or B=$Ga_{1-x}Al_xAs$ (x typ. ≤ 0.3)

Table 4.1. Semiconductor Material Parameters

Material	Periodic Table Classification	Bandgap Energy (eV)	Bandgap Wavelength (μm)	Exciton Bohr Radius (nm)	Exciton Binding Energy (meV)
CuCl	I–VII	3.395	0.36	0.7	190
CdS	II–VI	2.583	0.48	2.8	29
CdSe	II–VI	1.89	0.67	4.9	16
GaN	III–V	3.42	0.36	2.8	
GaP	III–V	2.26	0.55	10–6.5	13–20
InP	III–V	1.35	0.92	11.3	5.1
GaAs	III–V	1.42	0.87	12.5	5
AlAs	III–V	2.16	0.57	4.2	17
Si	IV	1.11	1.15	4.3	15
Ge	IV	0.66	1.88	25	3.6
$Si_{1-x}Ge_x$	IV	$1.15–0.874x + 0.376x^2$	$1.08–1.42x + 3.3x^2$	$0.85–0.54x + 0.6x^2$	$14.5–22x + 20x^2$
PbS	IV–VI	0.41	3	18	4.7
AlN	III–V	6.026	0.2	1.96	80

Semiconductive material choice

Da Yu and Cardona
Fundamentals of Semicond.
Springer (1996)

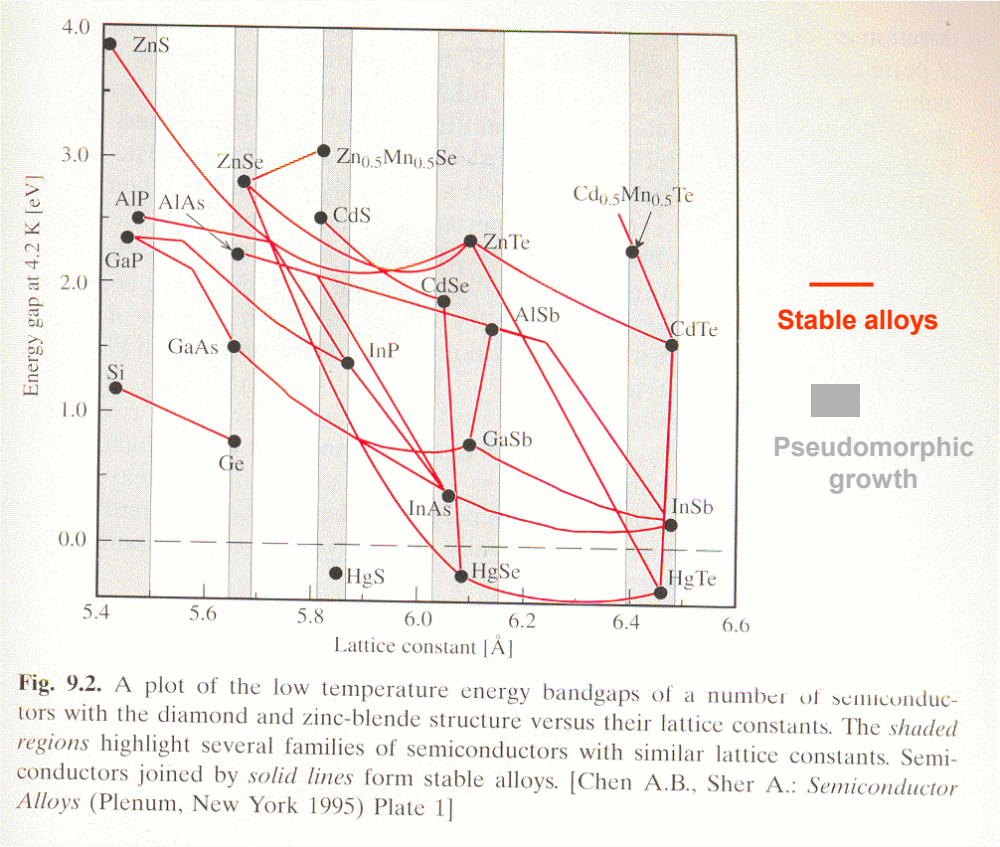

Fig. 9.2. A plot of the low temperature energy bandgaps of a number of semiconductors with the diamond and zinc-blende structure versus their lattice constants. The *shaded regions* highlight several families of semiconductors with similar lattice constants. Semiconductors joined by *solid lines* form stable alloys. [Chen A.B., Sher A.: *Semiconductor Alloys* (Plenum, New York 1995) Plate 1]

Now, higher gaps achieved with GaN

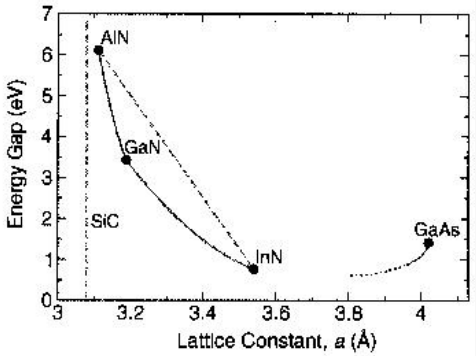

Figure 1. Fundamental bandgap versus basal-plane lattice constant of nitride materials compared with SiC and GaAs. The solid curves represent the ternary mixtures AlN/GaN,[10] GaN/InN,[11] and GaN/GaAs.[12] The dotted curve qualitatively indicates the continuation of the GaNAs gap toward GaN.

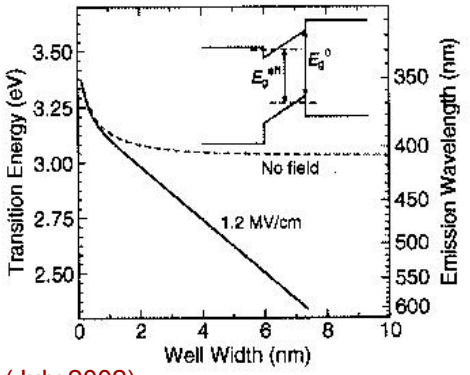

Figure 3. Transition energy of $Ga_{0.9}In_{0.1}N$/GaN quantum wells versus well width, with and without built-in electric field. The inset shows a schematic view of the band scheme, the effective bandgap E_g^{eff}, and the original bandgap E_g^0.

A wide choice of semiconductors is available to tune the gap in a broad range (from blue to near-IR)

See MRS Bull. 27 (July 2002)

Electroluminescent systems: lasers (and LEDs)

Basic ingredients for a laser:
-**Active medium** (amplification through stimulated emission);
-**Optical cavity** (feedback of the active medium for coherent emission)

Note: *if cavity is missing, an incoherent emitting device (i.e., a LED) is obtained*

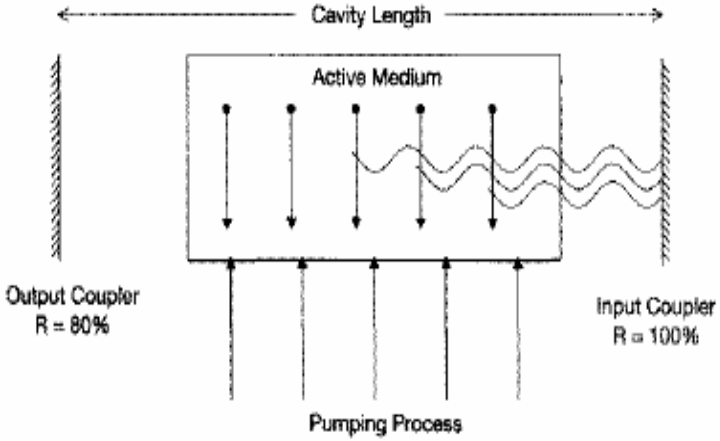

Figure 4.16. The schematics of a laser cavity. *R* represents percentage reflection.

In diode lasers (and LEDs) **pumping is achieved by electrical means**: current flow promotes electrons into the conduction band (and holes remain in the valence band) Electron/hole recombination leads to emission

Process is "enhanced" in the presence of excitons

If gain is large, couplers can be made of transitions between media having different refractive indexes (e.g., semiconductor/air)

"Conventional" diode lasers (with emission in a variety of spectral intervals) exploit quantum wells

Table 4.3. Quantum-Confined Semiconductors and the Lasing Wavelength Region

Quantum-Confined Active Layer	Barrier Layer	Substrate	Lasing Wavelength (nm)
InGaN	GaN	GaN	400–450
InGaP	InAlGaP	GaAs	630–650
GaAs	AlGaAs	GaAs	800–900
InGaAs	GaAs	GaAs	900–1000
InAsP	InGaAsP	InP	1060–1400
InGaAsP	InGaAsP	InP	1300–1550
InGaAs	InGaAsP	InP	1550
InGaAs	InP	InP	1550

“Conventional” (heterojunction) diode laser

In the case of a semiconductor quantum well laser, the active medium is a narrow bandgap semiconductor (e.g., GaAs) that is sandwiched between a *p*-doped (excess holes) AlGaAs and an n-doped (excess electrons) AlGaAs barrier layer. However, in most semiconductor lasers, the doped layers of AlGaAs are separated from GaAs by a thin undoped layer of same composition AlGaAs. The cavity is formed by the cleaved crystal surfaces that act as reflectors. The general principle for the semiconductor lasers can be illustrated by the schematic shown in Figure 4.17 for a double heterostructure semiconductor laser. The ohmic contacts on the top and bottom inject electrons and holes into the active region, which in this design is significantly thicker (>100 nm) than a quantum well. The electrons and holes combine in the active region (GaAs in the present case) to emit a photon. The threshold current density (current per cross-sectional area) is defined as the current density required for the onset of stimulated emission and hence lasing. At this current density, the optical gain produced in the medium by stimulated emission just balances the optical loss due to various factors (e.g., scattering, absorption loss, etc.). A thick active layer in the double heterostructure also acts as a waveguide to confine the optical waves. The output emerges from the edges, hence this configuration is also referred to produce edge emitting laser action.

The case of a quantum well laser, where a single quantum well of dimensions <10 nm (depends on the material) is used as the active layer, is referred to as SQW (single quantum well) laser. This thickness is too small to confine the optical wave, which then leaks into the confining barrier region. To simultaneously confine the carriers in the quantum well and the optical wave around it, one uses a layer for optical confinement in which the quantum well is embedded.

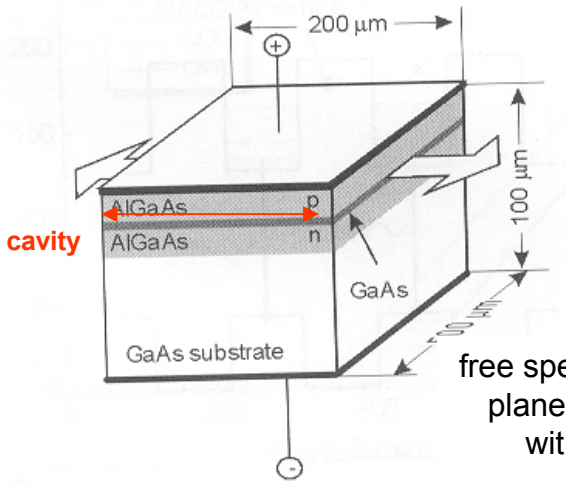

free spectral range for a plane-parallel cavity with length = L

$\Delta\nu = c/2L$

Figure 4.17. Scheme of double heterostructure semiconductor (DHS) lase

MQW frequently used as the active medium in order to enhance amplification (and reduce the threshold current)

Conventional semiconductor laser:

Light is generated across material's band-gap

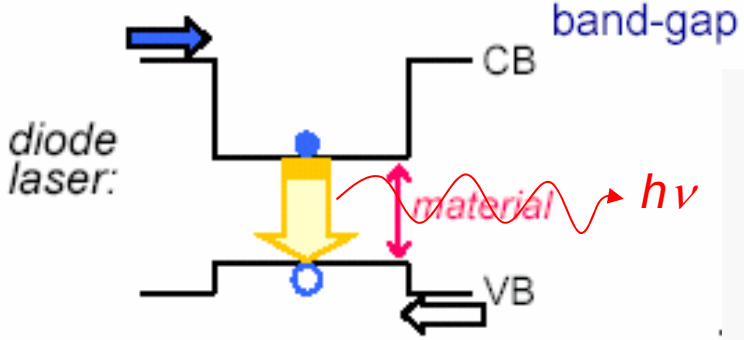

"Nanotechnological" diode lasers I: QD

C.P.Poole F.J.Owens
Introd. to Nanotechnology
(Wiley, 2003)

$\lambda = 1.32\ \mu m$

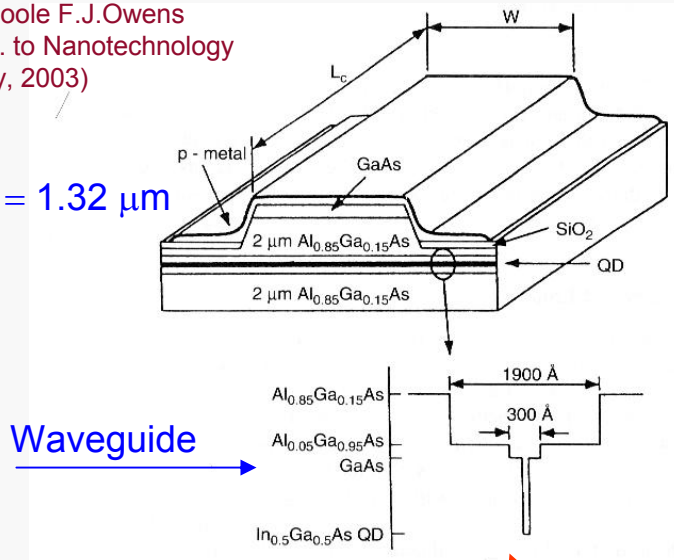

Figure 9.24. Schematic illustration of a quantum dot near-infrared laser. The inset at the bottom shows details of the 190-nm-wide ($Al_{0.85}Ga_{0.15}As$ cladded) waveguide region that contains the 12 monolayers of $In_{0.5}Ga_{0.5}As$ quantum dots (indicated by QD) that do the lasing. [From Park et al. (1999).]

Figure 9.24 provides a schematic illustration of a quantum-dot laser diode grown on an n-doped GaAs substrate (not shown). The top p-metal layer has a GaAs contact layer immediately below it. Between this contact layer above and the GaAs substrate (not shown) below the diagram, there are a pair of 2-μm-thick $Al_{0.85}Ga_{0.15}As$ cladding or bounding layers that surround a 190-nm-thick waveguide made of $Al_{0.05}Ga_{0.95}As$. The waveguide plays the role of conducting the emitted light to the exit ports at the edges of the structure. Centered in the waveguide (dark orizontal stripe on the figure labeled QD) is a 30-nm-thick GaAs region, and entered in this region are 12 monolayers of $In_{0.5}Ga_{0.5}As$ quantum dots with a ensity of $1.5 \times 10^{10}/cm^2$. The inset at the bottom of the figure was drawn to epresent the details of the waveguide region. The length L_C and the width W varied omewhat from sample to sample, with L_C = ranging from 1 to 5 mm, and W varying etween 4 and 60 μm. The facets or faces of the laser were coated with $ZnSe/MgF_2$ igh-reflectivity (> 95%) coatings that reflected the light back and forth inside tc ugment the stimulated emission. The laser light exited through the lateral edge o ıe laser.

Because of discrete features in the density of states, the quantum dot lasers have a very narrow gain curve and thus can be operated at even lower drive current and lower threshold current density compared to quantum wells (Arakawa, 2002). Figure 4.19 illustrates these features by comparing a quantum well laser with a quantum dot laser. It shows that for any output power, the drive current for a quantum dot laser is lower than that for a quantum well laser. Another important factor is temperature dependence. The quantum dot lasers, because of the widely separated discrete quantum states, show much more tolerance for temperature variation, compared to quantum well lasers. Since the first report of self-assembled InAs/InGaAs quantum dot lasers showing reduced temperature dependence of the threshold current (Bimberg et al., 1997), many other quantum dot lasers have been demonstrated. A more recent advancement is the report of InGaN quantum dots epitaxially grown on GaN to produce lasing action at room temperature (Krestnikov et al., 2000a,b).

In order for quantum dot lasers to compete with quantum well lasers, two major issues have to be addressed. Since the active volume provided by a single quantum dot is extremely small, a large array of quantum dots have to be used. A major challenge here is to produce an array of quantum dots with a very narrow size distribution to reduce inhomogeneous broadening and that are without defects that degrade

Da P.N. Prasad,
Nanophotonics,
Wiley (2004)

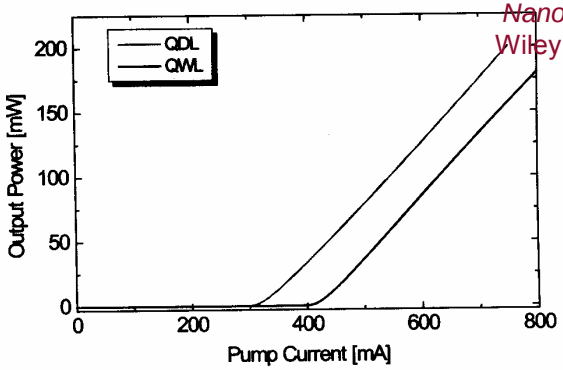

Figure 4.19. Comparison of efficiency between a quantum well laser and a quantum dot laser.

QD lasers appealing for enhanced gain (but fabrication of QD arrays is far from obvious)

See MRS Bull. 27 (July 2002)

"Nanotechnological" diode lasers II: VCSEL

Distributed Bragg Reflector structure (*1D photonic crystal*)

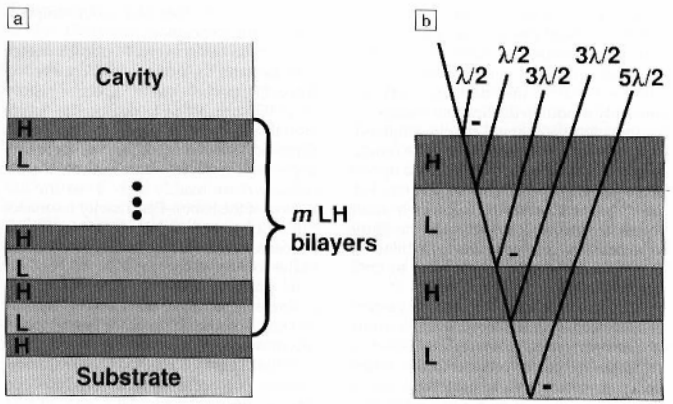

Figure 1. (a) Distributed Bragg reflector (DBR) structure using a high-refractive-index quarter-wave layer on the substrate followed by m low-index/high-index (LH) quarter-wave bilayers. (b) Relative phases at the DBR surface of light rays reflected from each interface within the DBR structure. The minus sign indicates the 180° phase shift that occurs upon reflection from a low- to high-index surface. A round-trip pass through each quarter-wave layer results in a half-wave phase shift. Every reflected ray returns to the DBR surface shifted by exactly 180° in phase. All reflected electric fields thus add constructively to give a high net reflectance for the DBR, even if individual interface reflectances are small.

Figure 2. Reflectance spectrum in air of a 1000-nm GaAs/AlAs DBR for 20 periods and 5 periods (lower two plots). Dashed lines show the reflectance from a bare GaAs substrate. Top plot shows the high-reflectance region of the 20-period mirror near the design wavelength.

"Bragg mirrors" can be built by depositing alternate layers with different refractive index and highly controlled thickness

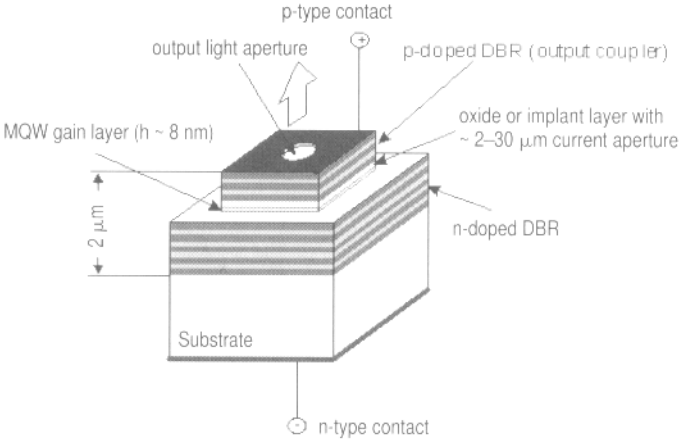

The laser cavity design discussed so far is that of an edge-emitting laser, also known as an in-plane laser, where the laser output emerges from the edge. However, many applications utilizing optical interconnection of systems require a high degree of parallel information throughput where there is a demand for surface emitting laser (SEL). In SEL the laser output is emitted vertically through the surface. Many schematics have been utilized to produce surface emitting lasers. A particularly popular geometry is that of a vertical cavity SEL, abbreviated as VCSEL. This geometry is shown in Figure 4.20. It utilizes an active medium such as multiple quantum wells sandwiched between two distributed Bragg reflectors (DBR), each comprising of a series of material layers of alternating high and low refractive indices. Thus for an InGaAs laser, the DBR typically consists of alternating layers of GaAs with refractive index ~3.5 and AlAs with refractive index 2.9, each layer being a quarter of a wavelength thick. These DBRs act as the two mirrors of a vertical cavity. Thus, both the active layer (InGaAs) and the DBR structures (GaAs, AlAs) can be produced in a continuous growth process.

An advantage offered by a VCSEL is that the lateral dimensions of the laser can be controlled, which offers the advantage that the laser dimensions can be tailored to match the fiber core for fiber coupling. An issue to deal with in VCSEL is the heating effect occurring in a complex multilayer structure, as the current is injected through a high series resistance of the DBRs.

Vertical Cavity Surface Emitting Laser

VCSEL advantages:

- **Surface emission for integration in optoelectronics;**
- **"short" cavity: temp. stability, beam optical features, ...;**
- **Small overall size, low threshold**

“Nanotechnological” diode lasers III: QC

Completely new approach to lasing action with the goals:
-Mid-IR lasers with possibility to engineer wavelength (e.g., for trace analysis);
-Huge efficiency (low threshold, high power)

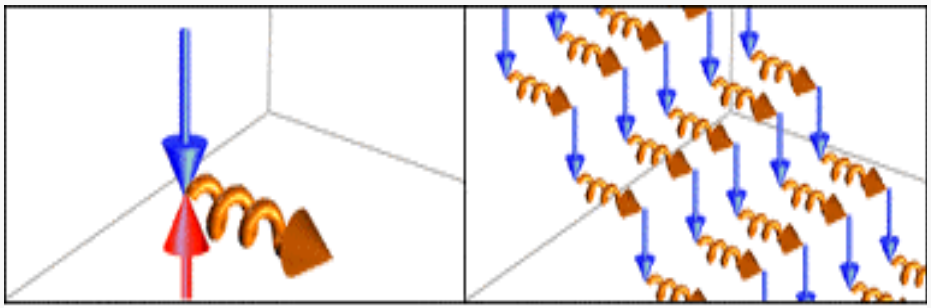

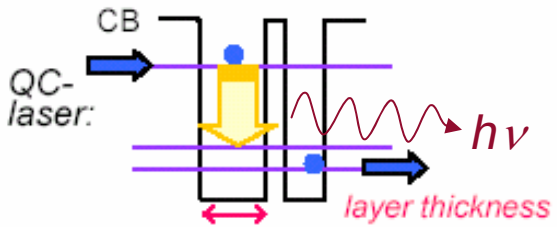

QC-laser:
Light is generated across designed energy ga
“materials by design”:
band structure engineering and MBE

- In contrast to the lasers discussed above, which involve the recombination of an electron in the conduction band and a hole in the valence band, the QC lasers use only electrons in the conduction band. Hence they are also called unipolar lasers.
- Unlike the quantum-confined lasers discussed above, which involve an inter-band transition between the conduction band and the valence band, the QC lasers involve intraband (inter-sub-band) transition of electrons between the various sub-bands corresponding to different quantized levels of the conduction band. These sub-bands have been discussed in Section 4.1.
- In the conventional laser design, one electron at the most can emit one photon (quantum yield one). The QC lasers operate like a waterfall, where the electrons cascade down in a series of energy steps, emitting a photon at each step. Thus an electron can produce 25–75 photons.

See http://www.unine.ch/phys/meso

Quantum Cascade lasers I

Figure 4.21 illustrates the schematics of the basic design principle of an earlier version of the QC lasers that produce optical output at 4.65 μm. These lasers are based on AlInAs/GaInAs. It consists of electron injectors comprised of a quantum well superlattice in which each quantized level along the confinement is spread into a miniband by the interaction between wells, which have ultrathin (1–3 nm) barrier layers. The active region is where the electron makes a transition from a higher sub-band to a lower sub-band, producing lasing action. The electrons are injected from left to right by the application of an electric field of 70 kV/cm as shown in the slope diagram. Under this field, electrons are injected from the ground state *g* of the miniband of the injector to the upper level 3 of the active region. The thinnest well in the active region next to the injector facilitates electron tunneling from the injector into the upper level in the active region. The laser transition, represented by the wiggly arrow, occurs between levels 3 and 2, because there are more electron populations in level 3 than in level 2. The composition and the thickness of the wells in the active region are judiciously manipulated so that level 2 electron relaxes quickly to level 1.

The cascading process can continue along the direction of growth to produce more photons. In order to prevent accumulation of electrons in level 1, the exit barrier of the active region is, again, made thin, which allows rapid tunneling of electrons into a miniband of the adjacent injector. After relaxing into the ground state *g* of the injector, the electrons are re-injected into the next active region. Each successive active region is at a lower energy than the one before; thus the active regions act as steps in a staircase. Therefore, the active regions and the injectors are engineered to allow the electrons to move efficiently from the top of the staircase to the

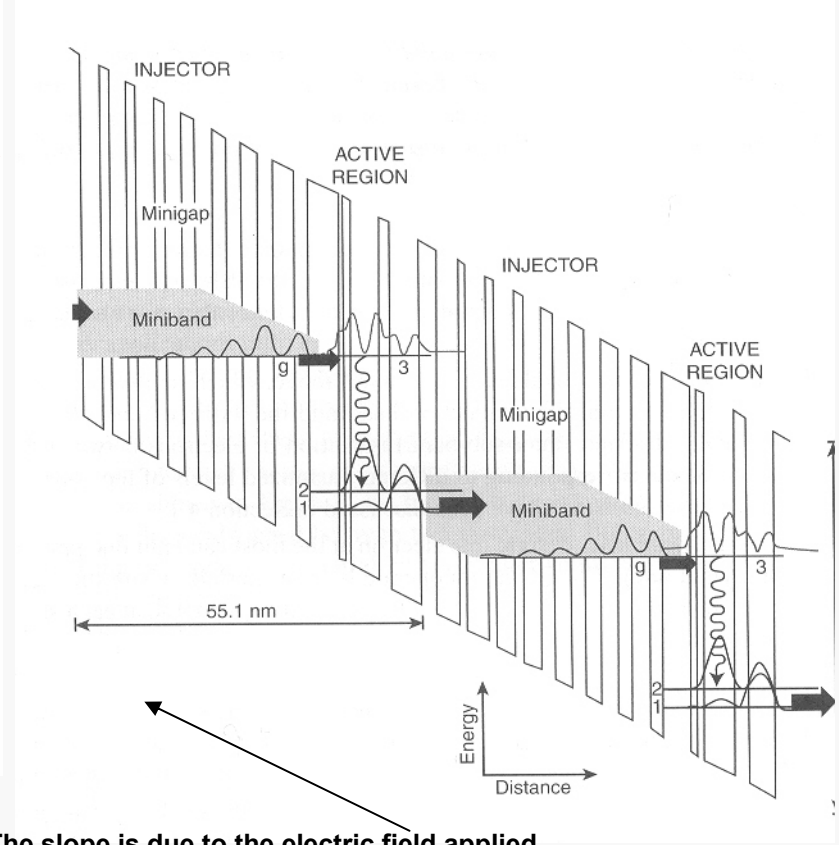

The slope is due to the electric field applied

Careful engineering and manufacturing of electron injector and active layers allow to achieve an efficient cascade behavior

Quantum Cascade lasers II

Quantum design of QC-laser

J. Faist, F. Capasso, C. Sirtori, D. L. Sivco, J. N. Baillargeon, A. L. Hutchinson, S. N. G. Chu, and A. Y. Cho, Appl. Phys. Lett. ***68****, pp. 3680-3682 (1996).*

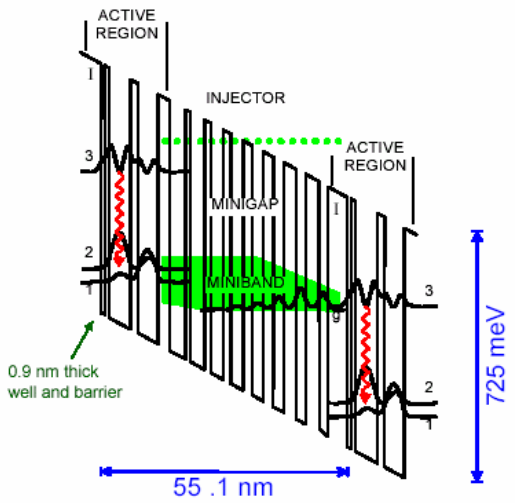

- multiple QWs under external applied electric field
- band-offset = 500 - 800 meV through lattice matched or strain-compensated n InP
- 1 - 100 active regions/injectors (typically ~ 30)
- layer thicknesses designed to provide population inversion $\tau_{32} >> \tau_2$
- designed for tunneling transport

Lucent Technologies
Bell Labs Innovations

Key characteristics of QC-lasers

- Wavelength ("color") determined by layer thickness rather than by material composition
- ➡ all mid-infrared spectrum covered by the same material
- Each electron creates N laser photons in traversing an N-stage cascaded structure (N = 20 - 75)
- ➡ intrinsically high power lasers
- High reliability: low failure rate, long lifetime and robust fabrication

Room temperature, pulsed, single-mode QC-DFB laser @ $\lambda \sim 4.65\ \mu m$

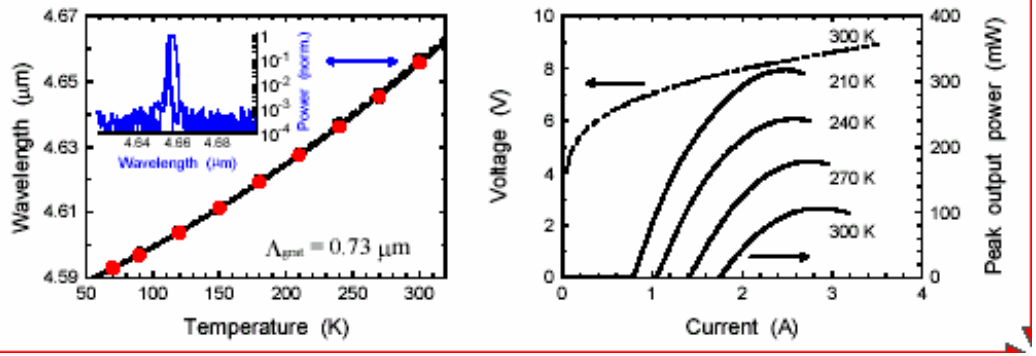

(es.:monitor for trace analysis of CO)

Wide wavelength-range of QC lasers

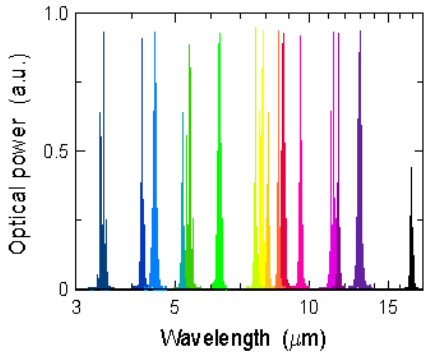

QC lasers cover entire mid-infrared wavelength range (3.4 - 17 μm) by tailoring layer thicknesses of the same material

Quantum Cascade lasers III

QC-laser crystal grown by Molecular Beam Epitaxy (MBE)

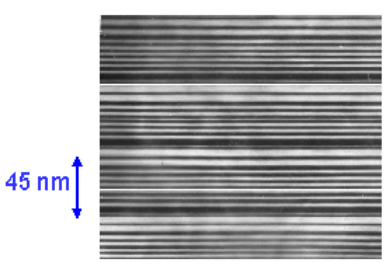

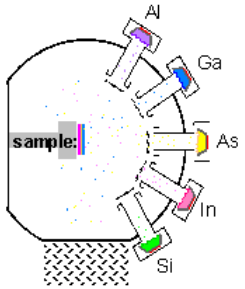

Cross-section of a few stages of QC-laser crystal ***crystal growth one atomic layer at a time***

- Many (~ 500), few-atoms thick layers of alloy materials (Al, Ga, As, In);
- atomic control of layer thickness, 1 nanometer (nm) = 4 atomic layers
- atomically flat layer interfaces

Ultra high purity MBE is the key for QC fabrication

TEM / SEM image

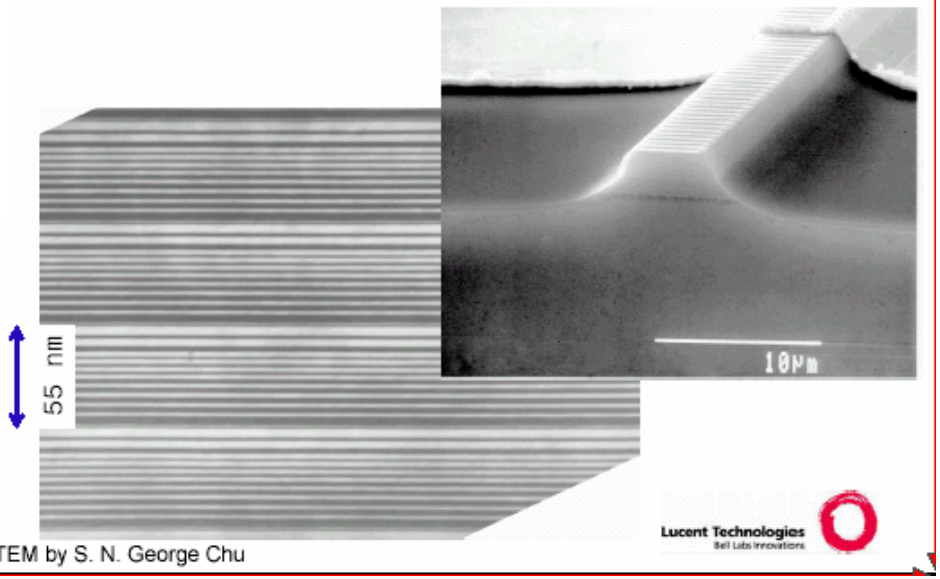

TEM by S. N. George Chu

Heterogeneous Cascades (multi-λ generation)

So far:

Homogeneous cascade:

single stack of ~ 30 *identical* active regions & injectors

Now:

Stacked cascades:

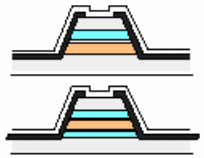

Different electric field across sub-stacks? - OK

Interdigitated cascades:

Charge transport between stages? - OK

Cooperative cascades:

How to design cooperation? see next VGs!

Lucent Technologies
Bell Labs Innovations

Further implementations

2. Quantum Dots and photoluminescence

4.1.3 Quantum Dots

Quantum dots represent the case of three-dimensional confinement, hence the case of an electron confined in a three-dimentional quantum box, typically of dimensions ranging from nanometers to tens of nanometors. These dimensions are smaller than the de Broglie wavelength thermal electrons. A 10-nm cube of GaAs would contain about 40,000 atoms. A quantum dot is often described as an artificial atom because the electron is dimensionally confined just like in an atom (where an electron is confined near the nucleus) and similarly has only discrete energy levels. The electrons in a quantum dot represent a zero-dimensional electron gas (0DEG). The quantum dot represents a widely investigated group of confined structures with many structural variations to offer. The size dependence of the lower excited electronic state of semiconductor nanocrystals has been a subject of extensive investigation for a long time (Brus, 1984). Quantum dots of all types of semiconductors listed in Table 4.1 have been made. Also, as we shall see in Chapter 7, a wide variety of methods have been utilized to produce quantum dots. Recent efforts have also focused on producing quantum dots in different geometric shapes to control the shapes of the potential barrier confining the electrons (and the holes) (Williamson, 2002).

A simple case of a quantum dot is a box of dimensions l_x, l_y, and l_z. The energy levels for an electron in such a case have only discrete values given as

$$E_n = \frac{h^2}{8m_e}\left[\left(\frac{n_x}{l_x}\right)^2 + \left(\frac{n_y}{l_y}\right)^2 + \left(\frac{n_z}{l_z}\right)^2\right] \qquad (4.7)$$

Energy

where the quantum numbers l_x, l_y, and l_z, each assuming the integral values 1, 2, 3, characterize quantization along the x, y, and z axes, respectively. Consequently, the density of states for a zero-dimensional electron gas (for a quantum dot) is a series of δ functions (sharp peaks) at each of the allowed confinement state energies.

$$D(E) \propto \sum_{E_n} \delta(E - E_n) \qquad (4.8)$$

1D DOS

In other words, $D(E)$ has discrete (nonzero) values only at the discrete energies given by Eq. (4.8). This behavior for $D(E)$ is also shown in Figure 4.3. The discrete values of $D(E)$ produce sharp absorption and emission spectra for quantum dots, even at room temperature. However, it should be noted that this is idealized, and the singularities are often removed by inhomogeneous and homogeneous broadening of spectroscopic transitions (see Chapter 6).

Another important aspect of a quantum dot is its large surface-to-volume ratio of the atoms, which can vary as much as 20%. An important consequence of this feature is strong manifestation of surface-related phenomena.

Quantum dots are often described in terms of the degree of confinement. The strong confinement regime is defined to represent the case when the size of the quantum dot (e.g., the radius R of a spherical dot) is smaller than the exciton Bohr radius a_B. In this case, the energy separation between the sub-bands (various quantized levels of electrons and holes) is much larger than the exciton binding energy. Hence, the electrons and holes are largely represented by the energy states of their respective sub-bands. As the quantum dot size increases, the energy separation between the various sub-bands becomes comparable to and eventually less than the exciton binding energy. The latter represents the case of a weak confinement regime where the size of the quantum dot is much larger than the exciton Bohr radius. The electron–hole binding energy in this case is nearly the same as in the bulk semiconductor.

Table 4.1. Semiconductor Material Parameters

Material	Periodic Table Classification	Bandgap Energy (eV)	Bandgap Wavelength (μm)	Exciton Bohr Radius (nm)	Exciton Binding Energy (meV)
CuCl	I–VII	3.395	0.36	0.7	190
CdS	II–VI	2.583	0.48	2.8	29
CdSe	II–VI	1.89	0.67	4.9	16
GaN	III–V	3.42	0.36	2.8	
GaP	III–V	2.26	0.55	10–6.5	13–20
InP	III–V	1.35	0.92	11.3	5.1
GaAs	III–V	1.42	0.87	12.5	5
AlAs	III–V	2.16	0.57	4.2	17
Si	IV	1.11	1.15	4.3	15
Ge	IV	0.66	1.88	25	3.6
$Si_{1-x}Ge_x$	IV	$1.15–0.874x + 0.376x^2$	$1.08–1.42x + 3.3x^2$	$0.85–0.54x + 0.6x^2$	$14.5–22x + 20x^2$
PbS	IV–VI	0.41	3	18	4.7
AlN	III–V	6.026	0.2	1.96	80

Important photoluminescence features in quantum dots

Si NC in porous Silicon

Bulk Si electrochemically etched in HF to produce (filamentary) nanocrystals

Electropolishing (large current):

$$Si + 6F^- \xrightarrow{+4e} SiF_6^{2-}$$

Porization (H surface evolution):

$$Si + 6F^- + 2H^+ \xrightarrow{+2e} SiF_6^{2-} + H_2$$

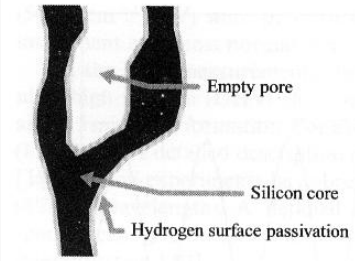

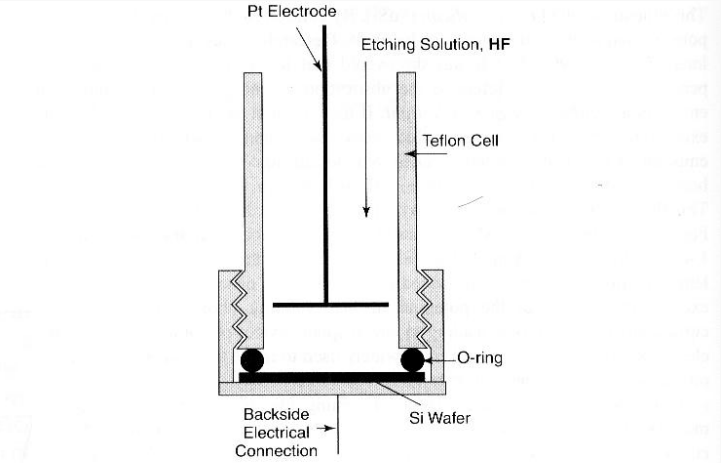

igure 6.21. A cell for etching a silicon wafer in a hydrogen fluoride (HF) solution in order to ıtroduce pores. (With permission from D. F. Thomas et al., in *Handbook of Nanostructured Materials and Nanotechnology*, H. S. Nalwa, ed., Academic Press, San Diego, 2000, Vol. 4, Chapter 3, p. 173.)

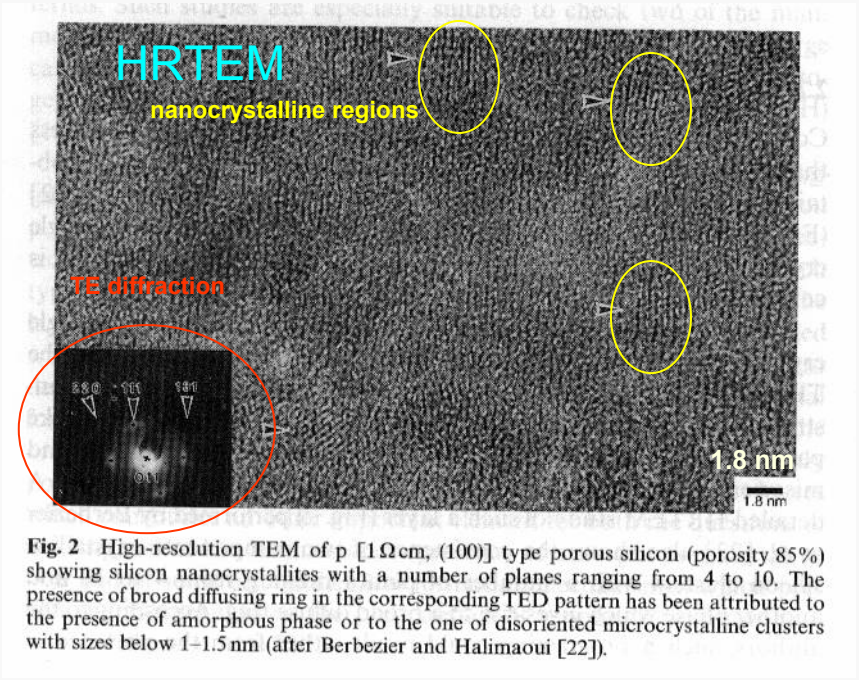

Fig. 2 High-resolution TEM of p [1 Ω cm, (100)] type porous silicon (porosity 85%) showing silicon nanocrystallites with a number of planes ranging from 4 to 10. The presence of broad diffusing ring in the corresponding TED pattern has been attributed to the presence of amorphous phase or to the one of disoriented microcrystalline clusters with sizes below 1–1.5 nm (after Berbezier and Halimaoui [22]).

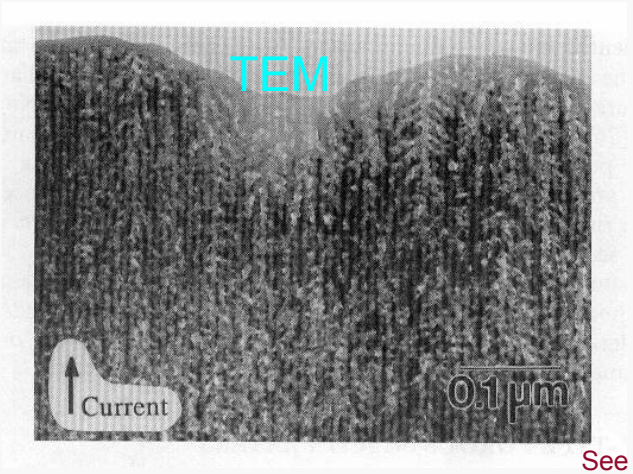

See Amato et al.
Struct. and Opt. Prop. of Po-Si nanostructures
(Gordon and Breach (1997)

Photoluminescence of po-Si

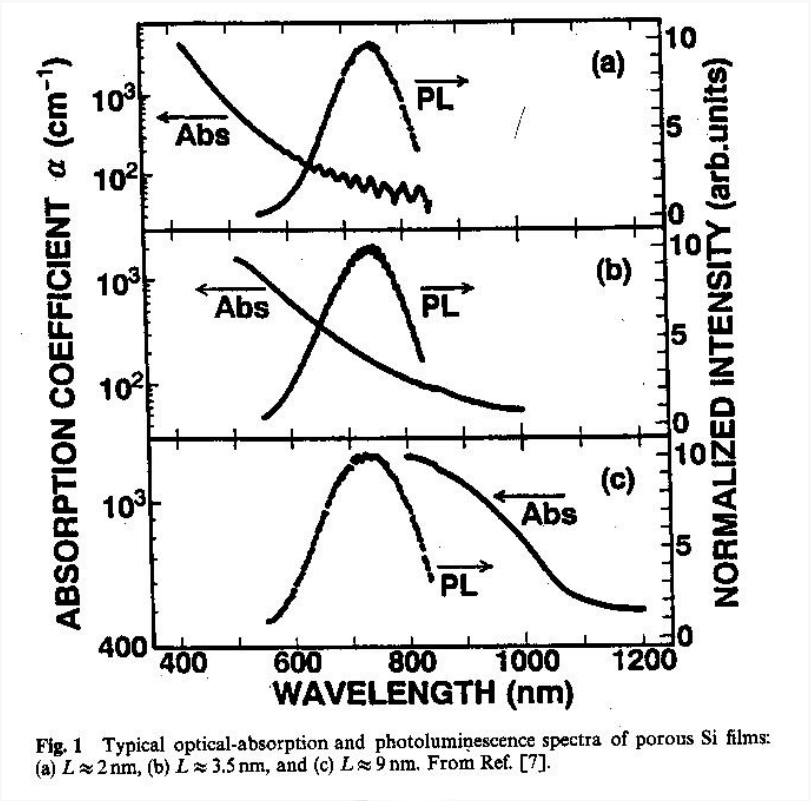

Fig. 1 Typical optical-absorption and photoluminescence spectra of porous Si films: (a) $L \approx 2$ nm, (b) $L \approx 3.5$ nm, and (c) $L \approx 9$ nm. From Ref. [7].

SNOM analysis of PL from po-Si microcavity

Da F.F. et al., J. Appl. Phys 91 5405 (2002)

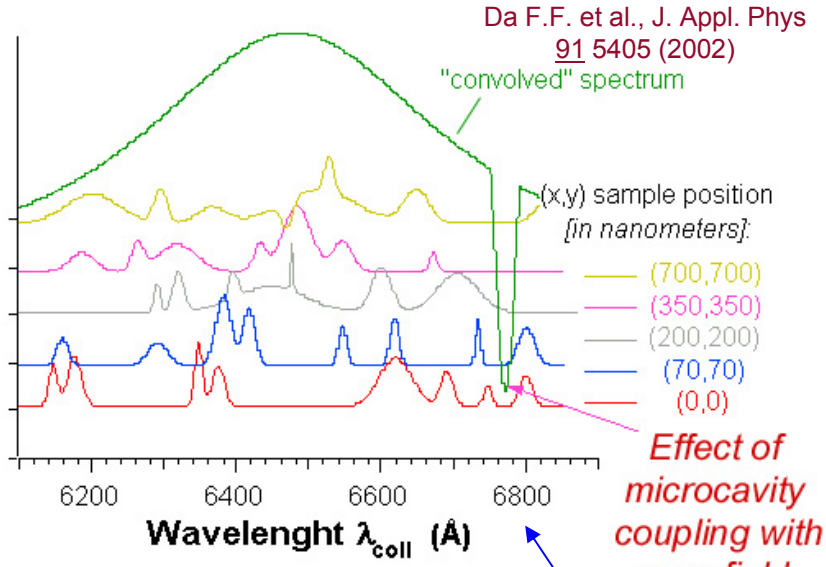

Emitting centers detected by SNOM

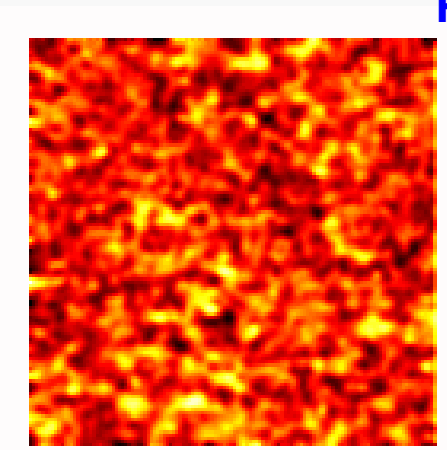

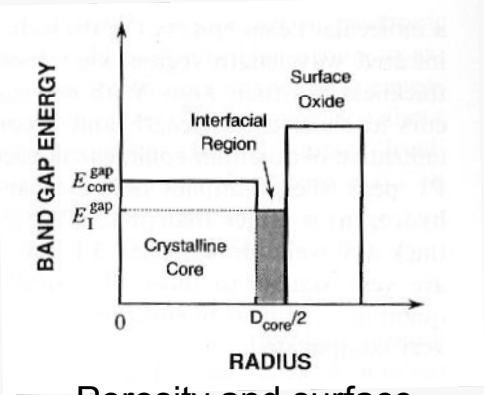

Porosity and surface passivation play a role

Even Si, in NC state, can lead to strong PL

NC in colloidal solutions

CdSe nanocrystals in solution

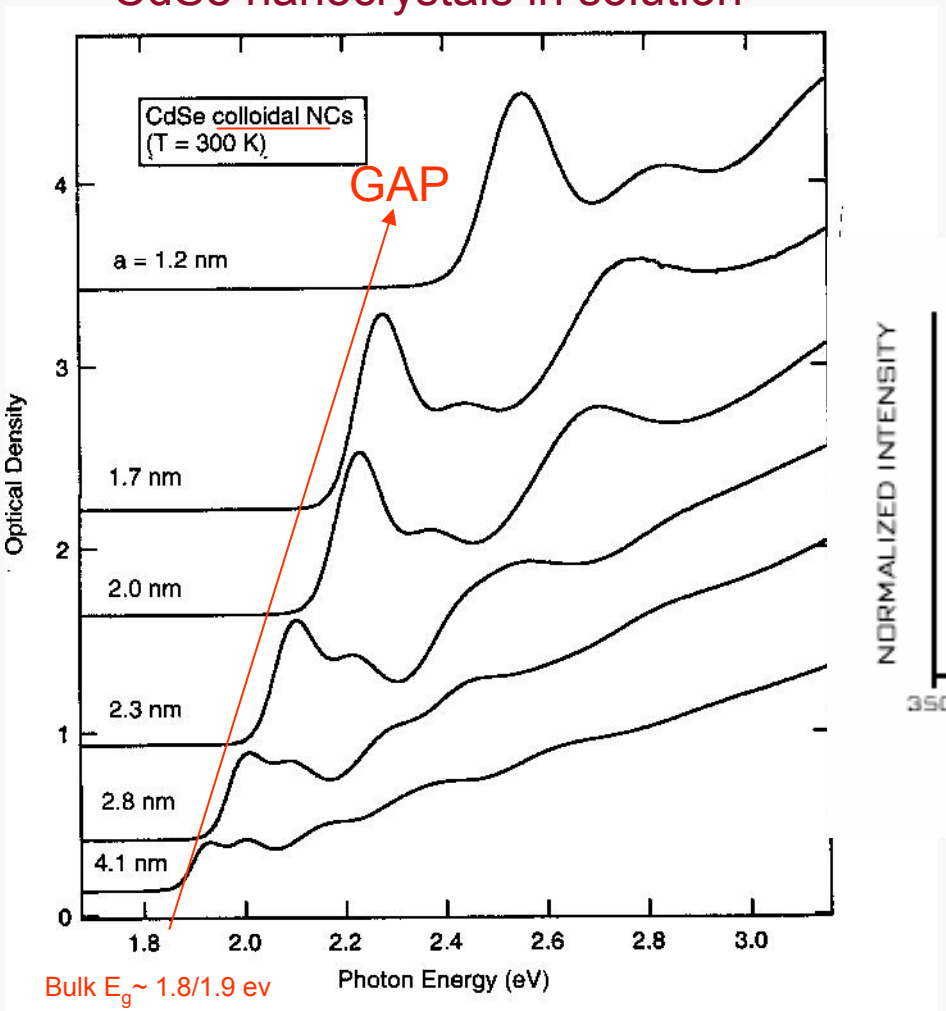

Bulk E_g~ 1.8/1.9 ev

ure 3.27. Room-temperature optical absorption spectra for CdSe colloidal nanocrystals
Cs) with mean radii in the range from 1.2 to 4.1 nm. [From V. I. Klimov, in Nalwa (2000),
l. 4, Chapter 7, p. 464.]

C.P.Poole F.J.Owens
Introd. to Nanotechnology
(Wiley, 2003)

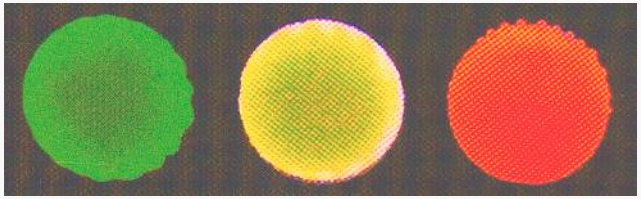

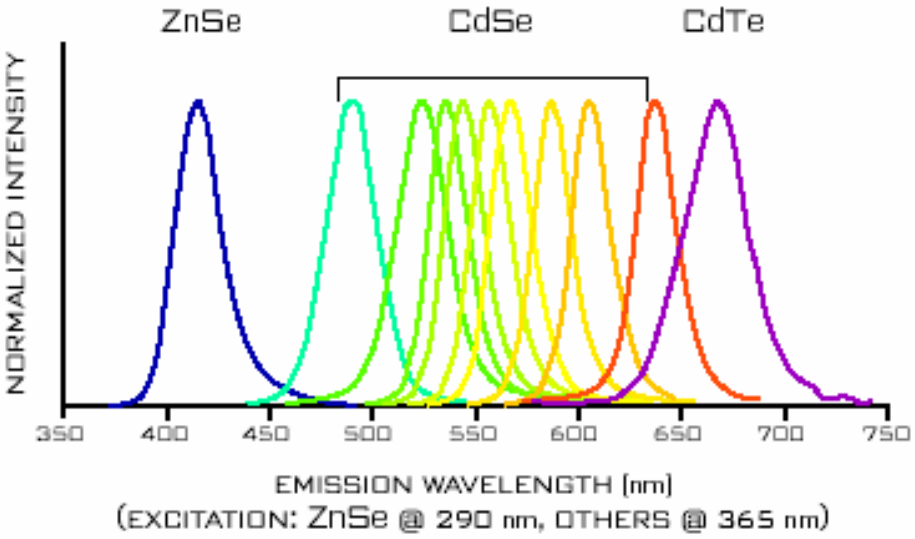

Wide "tunability" of PL range

QDs nanoislands on surfaces

AFM images

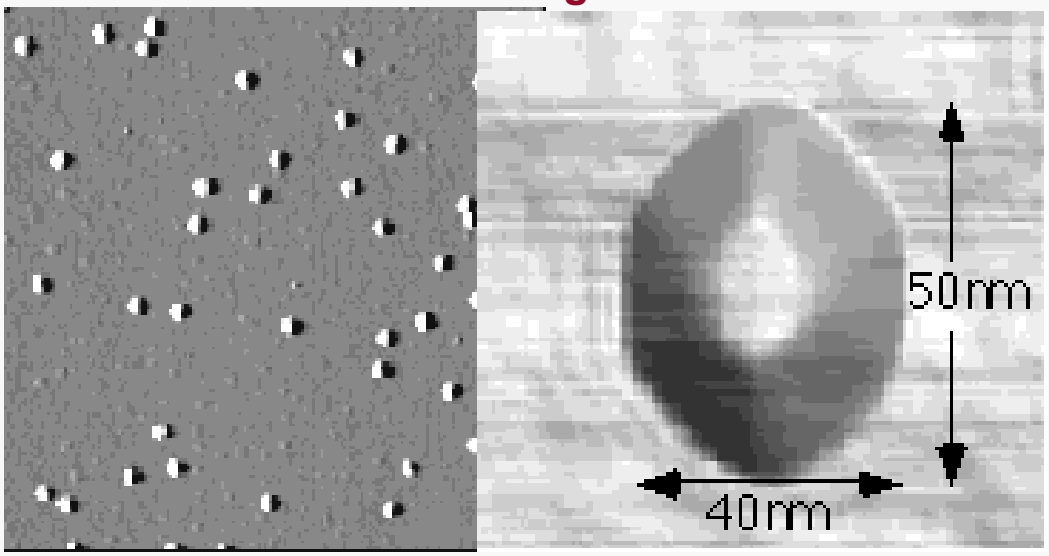

InP islands grown on and capped with InGaP (fabricated via MetallOrganic VaporPhaseEpitaxy)

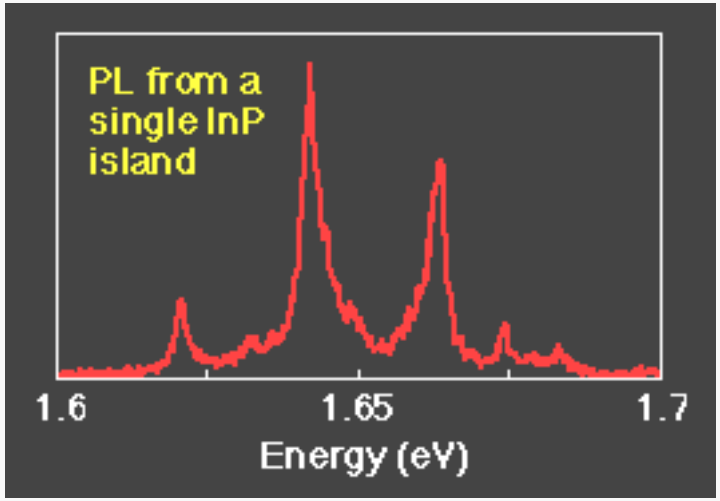

Spectral signatures of excitonic behavior:
sharp and strong PL (observed at room temp)

See Hessmann et al. APL 68 (1996)

Bulk E_g~ 1.5 ev

Core/shell Quantum Dots

This section describes semiconductor nanostructures that consist of a quantum dot core with one or more overlayers of a wider bandgap semiconductor. The core-shell quantum dots consist of a quantum dot with one overcoating (shell) of a wider bandgap semiconductor (Wilson et al., 1993; Hines and GuyotSionnest, 1996). The quantum dot–quantum well (QDQW) structure involves an onion-like nanostructure composed of a quantum dot core surrounded by two or more shells of alternating lower and higher bandgap materials (Schooss et al., 1994). These types of hierarchical nanostructures introduce a new dimension to bandgap engineering (modifications of the bandgap profile, charge-carrier properties, and luminescence feature). In the case of a core-shell structure, changing the shell can be used to manipulate the nature of carrier confinement in the core, thus affecting the optical properties. Furthermore, an overcoating with a wider bandgap semiconductor passivates the surface nonradiative recombination sites, thereby improving the luminescence efficiency of the quantum dot. In the case of QDQW structures, additional tuning of the energy levels and carrier wavefunctions can be obtained by varying the nature and the width of the quantum well surrounding the quantum dot.

Numerous reports of core-shell quantum dots exist. Some examples are ZnS (shell) on CdSe (quantum dots) (Dabbousi et al., 1997; Ebenstein et al., 2002), CdS on CdSe (Tian et al., 1996; Peng et al., 1997), ZnS on InP (Haubold et al., 2001), and $ZnCdSe_2$ on InP (Micic et al., 2000). The use of a wider bandgap semiconductor shell permits the light emitted from the core quantum dot to be transmitted through it without any absorption in the shell. These core-shell structures exhibit many interesting modifications of their luminescence properties. As an example, the results reported by Dabbousi et al. for the CdSe–ZnS core-shell quantum dots are summarized below:

- A small red shift in the absorption spectra of the core-shell quantum dot compared to that for the bare quantum dot is observed. This red shift is explained to arise from a partial leakage of the electronic wave function into the shell semiconductor. When a ZnS shell surrounds the CdSe quantum dot, the electron wavefunction is spread into the shell but the hole wavefunction remains localized in the quantum dot core. This effect produces a lowering of the bandgap and consequently a red shift. The red shift becomes smaller when the difference between the bandgaps of the core and the shell semiconductor increases. Hence, a CdSe–CdS core-shell structure exhibits a large red shift compared to the bare CdSe quantum dot of the same size (CdSe core). Also, the red shift is more pronounced for a smaller-size quantum dot where the spread of the electronic wavefunction to the shell structure is increased.
- For the same size CdSe quantum dot (~4 nm), as the coverage of the ZnS overlayer increases, the photoluminescence spectra show an increased red shift of emission peak compared to the absorption peak, with an increase in broadening. This effect may arise from an inhomogeneous distribution of the size and preferential absorption into larger dots. The photoluminescence quantum yield first increases with the ZnS coverage reaching to 50% at approximately ~1.3 monolayer coverage. At higher coverage, it begins to decrease. The increase in the quantum yield is explained to result from passivation of surface vacancies and nonradiative recombination sites. The decrease at higher coverage was suggested to arise from defects in the ZnS shell producing new nonradiative recombination sites.

The reported core-shell structure fabrication methods have utilized procedures for formation of the core (quantum dots) which produce polydispersed samples of core nanoparticles. These core particles then must be size-selectively precipitated before overcoating, making the process inefficient and time-consuming.

More recently, we developed a rapid wet chemical approach to produce core-shell structures using novel chemical precursors which allows us to make III–V quantum dots (a more difficult task than the preparation of II–VI quantum dots) rapidly, (less than two hours) (Lucey and Prasad, 2003). Then without the use of surfactants or coordinating ligands, the quantum dots are overcoated by the shells rapidly using inexpensive and commercially available II–VI precursors that are not air-sensitive. This process was used to produce CdS on InP, CdSe on InP, ZnS on InP, and ZnSe on InP. The optical properties of these core-shell structures were strongly dependent on the nature of the shell around InP. A ZnS shell around the

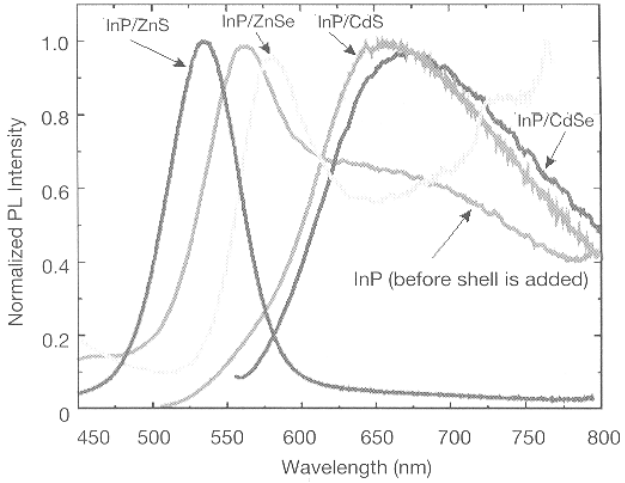

Figure 4.14. Photoluminescence spectra of InP quantum dots and the various core-shell structures involving InP core of some diameter (~3 nm).

Functionalization of core/shell QDs

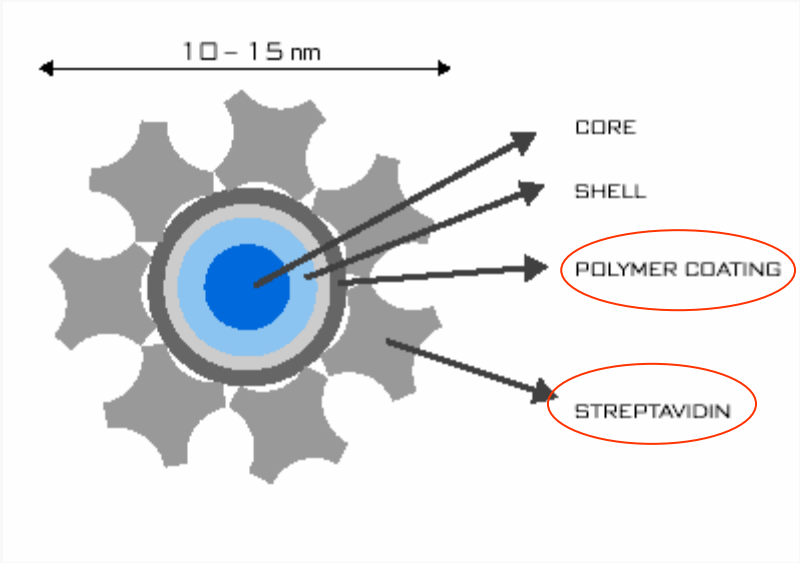

http://faculty.washington.edu/stenkamp/strep.html

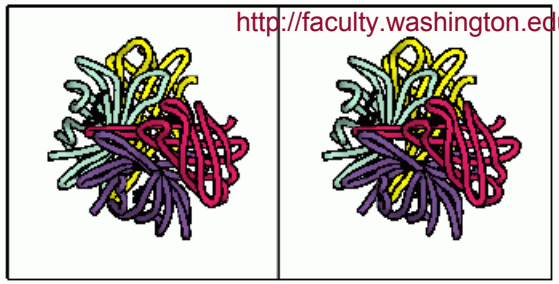

See www.qdots.com

Above is a stereoview of the streptavidin tetramer showing the subunit arrangement and the biotin binding site.

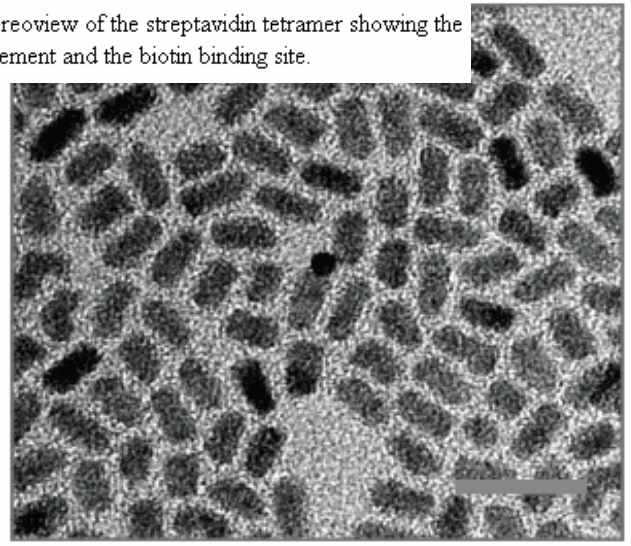

Electron Micrograph. Transmission electron microscopy can be used to directly image Qdot core-shell nanocrystals. The darker regions are the crystallites. Like several of QDC's products, these core-shell nanocrystals are rod-like in structure. The magnification is 200,000 and the scale bar is 20 nm.

Preparazione:
Core (CdSe)
$Cd(CH_3)_2$ e Se in TBP o TOP
reazione a 360°C e raffreddata 290°C, temp ambiente
controllo crescita tramite spettro di assorbimento
Shell (ZnS)
$(TMS)_2S$ e $Zn(Et)_2$ in TOP
reazione a 190°C
controllo crescita spettroscopia UV-Vis e fotoluminscenza

Materiale tratto dal seminario di Marco Cirillo, Apr. 2004

The shell can be further functionalized in order to be compatible with organics

Fluorescence marker applications

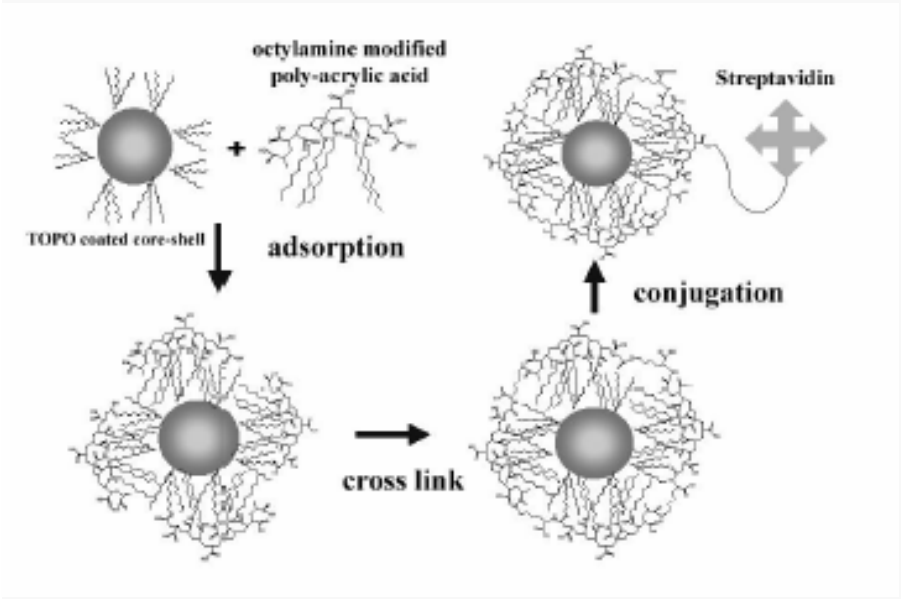

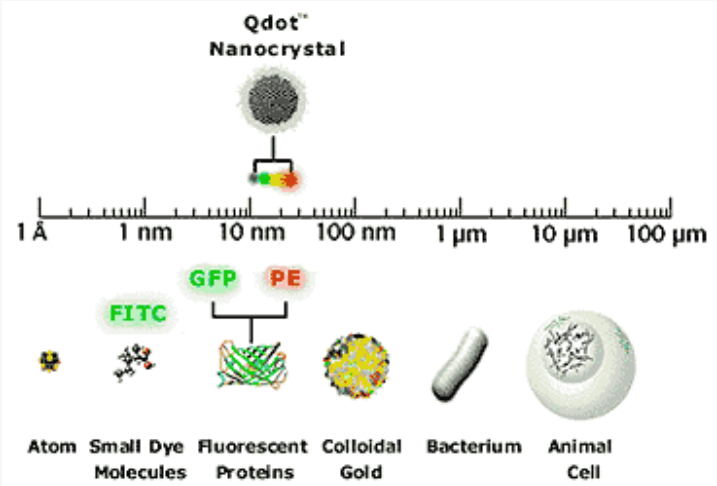

QDs preferred to molecular dyes for:
-Larger quantum efficiency;
-Larger “compatibility”;
-High degree of versatility

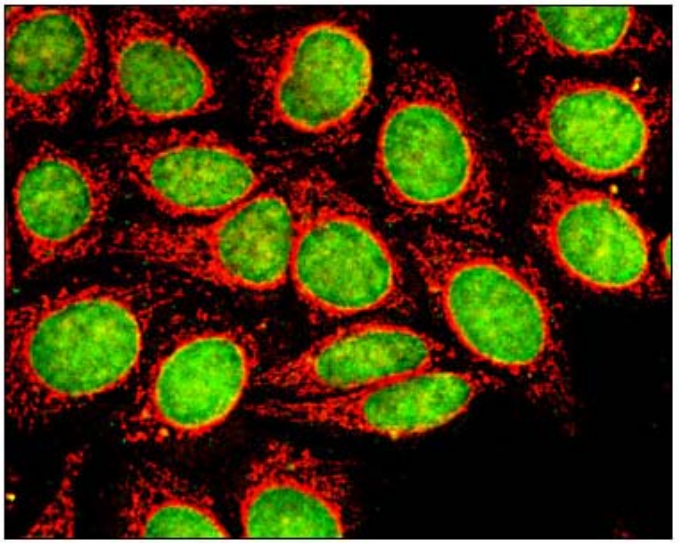

See www.qdots.com

Figure 1. Fluorescent double-labeling with Qdot Streptavidin Conjugates. Fixed human epithelial cells were incubated with a mixture of human anti-mitochondria antibodies and mouse anti-histone antibody. The mitochondria were labeled with Qdot 605 Streptavidin Conjugate (red) after the specimens were incubated with biotinylated goat anti-human IgG. The cells then were blocked with biotin solution, incubated with biotinylated goat anti-mouse IgG and the nuclei were stained with Qdot 525 Streptavidin Conjugate (green).

3. Optical behavior of metal nanoparticles I

Mysterious red color in Lycurgus Cup

Dr. Juen-Kai Wang

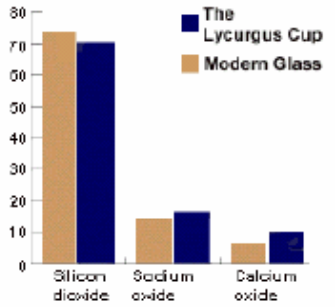

The same composition as modern glass

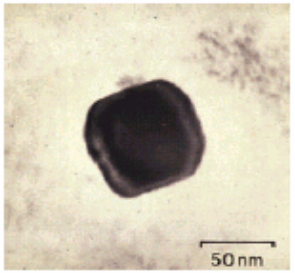

X-ray analysis: 70% Ag + 30% Au

These Ag-Au nanoparticles (~300 ppm) scatter the light, rather in the same way that fine particles in the atmosphere cause a 'red sky at night' effect. They cause the color effects shown by the Cup.

The Lycurgus Cup, Roman (4th century AD), British Museum (www.thebritishmuseum.ac.uk)

See: http://www.ndhu.edu.tw /~nano/93041702.pdf

Gold Building Blocks

Atoms: colorless, 1 Å

Gold clusters: orange, nonmetallic, <1 nm

Gold nanoparticles: 3–30 nm, red, metallic, "transparent"

Gold particles: 30–500 nm metallic, turbid, crimson to blue

Bulk gold film

Figure 1. Gold building blocks, from the atomic to the mesoscopic, and their changing colors.

Au nanoparticles in solution

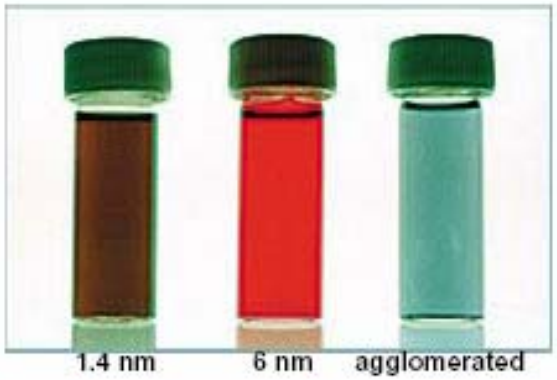

Reminders of plasma frequency and e.m. waves in metals I

ONDE IN UN MEZZO CONDUTTORE

Fissata la frequenza ω per un' onda e.m. piana di questa frequenza abbiamo: $\dot{\vec{E}} = \frac{\partial \vec{E}}{\partial t} = -i\omega\vec{E}$.

Naturalmente ci siamo riferiti alla notazione complessa dell' onda $\vec{E} = \vec{E}_0 e^{i(\vec{k}\cdot\vec{r}-\omega t)} = E_0 e^{i(kz-\omega t)}\hat{i}$ avendo scelto, per maggiore chiarezza, l' asse z lungo $\vec{k}$ e l' asse x lungo $\vec{E}_0$.

Se l'onda si propaga in un mezzo conduttore di conducibilita' σ, nel materiale sara' presente una densita' di corrente $\vec{j} = \sigma\vec{E}$. L'equazione di Maxwell $rot\vec{H} = \vec{J} + \frac{\partial \vec{D}}{\partial t}$ potra' allora essere riscritta come: $rot\vec{H} = \sigma\vec{E} + \varepsilon_0\varepsilon\dot{\vec{E}} = \sigma\frac{\dot{\vec{E}}}{-i\omega} + \varepsilon_0\varepsilon\dot{\vec{E}}$ e, in definitiva:

$$rot\vec{H} = \varepsilon_0(\varepsilon + i\frac{\sigma}{\varepsilon_0\omega})\dot{\vec{E}}$$

Si vede allora che basta considerare una nuova costante dielettrica per il materiale: alla ε, che e' il contributo delle cariche legate, bisogna aggiungere il contributo delle cariche libere e cioe' quello che nasce dalla conduzione.

Alle frequenze "basse" sia ε che σ sono reali (e positivi). Nei metalli $\sigma \approx 10^8(\Omega\cdot m)^{-1}$ ed $\varepsilon \approx 1$ per cui, tenendo conto del valore di ε_0, si vede che, fino a frequenze dell' ordine di 10^{14}, si puo' trascurare ε e tenere solo il contributo delle cariche libere $i\frac{\sigma}{\varepsilon_0\omega}$. Inoltre, fino a frequenze dell' ordine di quelle delle microonde, la conducibilita' e' indipendente dalla frequenza ed e' circa uguale alla conducibilita' statica σ_0. Riscrivendo semplicemente quanto gia' trovato nel caso dei dielettrici non magnetizzabili ($\mu \simeq 1$ e' un caso generalissimo) si ottiene: $k = \frac{\omega}{c}\sqrt{\varepsilon}$. Essendo $\sqrt{i} = \frac{1+i}{\sqrt{2}}$, si ha

$$\sqrt{\varepsilon} = n + i\beta = \sqrt{\frac{\sigma_0}{\varepsilon_0\omega}}\left(\frac{1+i}{\sqrt{2}}\right).$$

L'ultima espressione mostra che $n = \beta = \sqrt{\frac{\sigma_0}{2\varepsilon_0\omega}}$.

Introducendo il valore di k nell' onda da cui siamo partiti, avremo alla fine

$$\vec{E} = E_0 e^{i(kz-\omega t)} = E_0 e^{-\frac{\omega}{c}\beta z} e^{i(\frac{\omega}{c}nz-\omega t)}\hat{i}$$ e, da qui, e dalla $rot\vec{E} = -\dot{\vec{B}} \Rightarrow i\vec{k}\wedge\vec{E} = i\omega\vec{B}$,

$$\vec{B} = \frac{n+i\beta}{c}E_0 e^{-\frac{\omega}{c}\beta z} e^{i(\frac{\omega}{c}nz-\omega t)}\vec{j}$$

P.L. Braccini, Lezioni di Fisica II
Per ing. TLC (Pisa, 2001)

SIGNIFICATO FISICO DELLA FREQUENZA DI PLASMA.

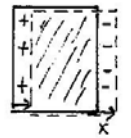

Supponiamo di essere in presenza di un gas completamente ionizzato: $n^+ = n^- = n$ sono le concentrazioni degli ioni positivi e degli elettroni per cui il gas risulta globalmente neutro.
Supponiamo anche di far subire agli elettroni uno spostamento x (piccolo) rispetto agli ioni positivi (come avviene nel processo di polarizzazione indotta da un campo elettrico). La situazione e' quella mostrata nella figura: la densita' superficiale delle cariche dei due segni che si e' creata sulle superfici e' nex per cui, nello spazio interno al volume, sara' presente un campo elettrico $E_x = \frac{nex}{\varepsilon_0}$. Ogni elettrone sara' quindi soggetto ad una forza elastica di richiamo

$F_x = -eE_x = -\frac{ne^2x}{\varepsilon_0}$ per cui, una volta lasciato libero, l'elettrone, e con lui tutto il plasma collettivamente, compira' oscillazioni di frequenza propria $\omega_0^2 = \frac{ne^2}{m\varepsilon_0}$ che e' proprio la frequenza di plasma. In presenza di una forza esterna periodica, come quella generata dal campo elettrico di un'onda e.m., ω_p e' la frequenza di risonanza. A questa frequenza l'energia sottratta all'onda sara' particolarmente elevata.

Si noti che la condizione $\omega\tau >> 1$ (e cioe' $\tau >> T$) indica che il periodo T della oscillazione del plasma e' molto piu' piccolo del tempo medio d'urto. Cio' vuol dire che gli elettroni effettueranno un gran numero di oscillazioni forzate di grande ampiezza e, alla fine, cederanno agli ioni tutta l'energia sottratta all' onda, energia che avevano nel frattempo accumulato sotto forma di energia cinetica.

IL MODELLO DI DRUDE DELLA CONDUCIBILITA' ELETTRICA

Correnti stazionarie

In questo modello il moto dell'elettrone dentro un metallo, viene continuamente reso casuale dagli urti con il reticolo entro cui l' elettrone si muove. Se dentro il metallo e' presente un campo elettrico medio $\vec{E}$ l'elettrone, fra due urti successivi, verra' accelerato da questo campo e l'equazione del moto dell'elettrone (massa m, carica $-e$) sara'

$$m\frac{d\vec{v}}{dt} = -e\vec{E}.$$

Al tempo $t = 0$, l' elettrone che aveva subito l'ultimo urto al tempo $-T$, avra' acquistato una velocita' $\vec{v} = \frac{-e\vec{E}}{m}T$. Mediando su tutti gli elettroni la velocita media sara' allora

$$<\vec{v}> = \frac{-e\vec{E}}{m}\tau$$

dove si e' indicato con τ il *tempo medio d' urto* e cioe' il valor medio di T calcolato su tutti gli elettroni.

Se n e' il numero di elettroni liberi per unita' di volume, la densita' di corrente sara'

$$\vec{J} = n(-e)<\vec{v}> = \frac{ne^2\tau}{m}\vec{E}.$$

La conducibilita' statica sara' allora:

$$\sigma_0 = \frac{ne^2\tau}{m}.$$

Nella maggior parte dei metalli $10^{-15}s < \tau < 10^{-14}s$.

Reminders of plasma frequency and e.m. waves in metals II

Campi variabili

Se invece di un campo statico e' presente nel metallo un' onda e.m. di frequenza ω, trasurando gli effetti magnetici (in generale molto piccoli), l' equazione per la velocita' media di un elettrone che si trovi nell' origine sara':

$$m\frac{d<\vec{v}>}{dt} = -m\gamma<\vec{v}> - e\vec{E}_0 e^{-i\omega t}.$$

A secondo membro l'ultimo termine e' la forza oscillante che il campo elettrico dell' onda esercita sull' elettrone, mentre il primo termine, una forza di smorzamento viscoso, e' stato introdotto per tener conto degli urti dell' elettrone con il reticolo. Si deve notare che si e' fatta l'ipotesi che il campo elettrico non vari apprezzabilmente su distanze dell' ordine degli spostamenti dell' elettrone durante il suo moto.

Cercando una soluzione in cui $<\vec{v}>$ oscilli con la stessa frequenza ω si trova:

$$<\vec{v}> = \frac{-eE_0 e^{-i\omega t}}{m(\gamma - i\omega)}.$$

Da qui: $\vec{j} = n(-e)<\vec{v}> = \frac{ne^2\vec{E}}{m(\gamma - i\omega)}$ per cui

$$\sigma(\omega) = \frac{ne^2}{m(\gamma - i\omega)}.$$

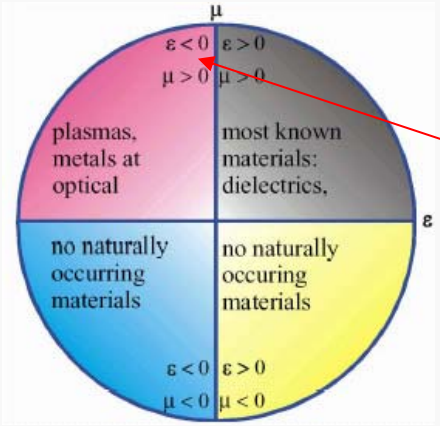

Metal response at optical wavelengths: ε < 0

Se si vuole che a frequenza zero, questo risultato riproduca la σ_0 statica, si vede che deve essere $\gamma = \frac{1}{\tau}$.

Si puo' scrivere in definitiva $\sigma(\omega) = \frac{\sigma_0}{1 - i\omega\tau}$.

La conducibilita' a basse e ad alte frequenze.

Ricordando che nei metalli $\tau \sim 10^{-14}\,s$ si vede che, almeno fino alle frequenze delle microonde $(\omega < 10^{11}\,s^{-1})$, la conducibilita' e' indipendente dalla frequenza ed il suo valore e' uguale alla conducibilita' statica σ_0.

Quando invece $\omega\tau >> 1$, e cioe' per $\omega >> 10^{14}\,s^{-1}$ (frequenze dell' ultravioletto), si puo' scrivere:

$$\sigma(\omega) = i\frac{\sigma_0}{\omega\tau}.$$

Nei metalli, a queste frequenze, il contributo delle cariche libere alla costante dielettrica diviene allora

$$\frac{i\sigma(\omega)}{\varepsilon_0\omega} \simeq -\frac{\sigma_0}{\varepsilon_0\omega^2\tau} = -\frac{\omega_p^2}{\omega^2}$$

dove abbiamo introdotto un nuovo parametro, la *frequenza di plasma* ω_p definita da

$$\omega_p^2 = \frac{\sigma_0}{\varepsilon_0\tau} = \frac{ne^2}{\varepsilon_0 m}.$$

La frequenza di plasma caratterizza il materiale conduttore; non dipende da τ, ma dipende solamente dalla densita' n dei portatori di carica. Nella maggior parte dei metalli $\omega_p \sim 10^{16}\,s^{-1}$. Nell'ultravioletto, sempre per i metalli, il contributo alla costante dielettrica delle cariche legate e' molto piccolo, per cui $\varepsilon(\omega)_{legate} \simeq 1$. La costante dielettrica complessa e' allora :

$$\varepsilon(\omega) \simeq 1 - \frac{\omega_p^2}{\omega^2}.$$

Per quanto riguarda la propagazione di onde e.m. la frequenza di plasma costituisce allora una frequenza di riferimento precisa. Se la frequenza dell' onda e' $\omega < \omega_p$, la ε e' negativa per cui $\sqrt{\varepsilon}$ sara' immaginaria pura: *la propagazione nel mezzo e' impedita e l' onda, se incide sul metallo, verra' interamente riflessa.*

Se invece $\omega > \omega_p$, $\sqrt{\varepsilon}$ e reale: piu' precisamente $n = \sqrt{(1 - \frac{\omega_p^2}{\omega^2}}$ e $\beta = 0$ per cui *l'onda puo' propagarsi nel mezzo con attenuazione molto piccola* (nelle nostre approssimazioni l' attenuazione e' nulla).

Surface plasmons at a metal/dielectric interface I

Surface Plasmon Resonance (SPR) Theory: Tutorial

Masahiro Yamamoto
Department of Energy and Hydrocarbon Chemistry, Kyoto University,
Yoshida honmachi, Sakyo-ku, Kyoto, 606-8501, JAPAN

www.scl.kyoto-u.ac.jp/~masahiro/sprtheory.pdf

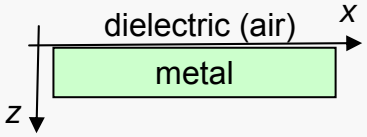

4 Surface Plasmon

The electronic charges on metal boundary can perform coherent fluctuations which are called surface plasma oscillations. The fluctuations are confined at the boundary and vanishes both sides of the metal surface. This plasmon waves have p-character because the surface charge induce the discontinuity of the electric field in the surface normal z-direction, but s-waves has only E_y component (no E_z component).

Now we consider the air(medium 2)|metal(medium 1) surface where the electric fields are dumped both side of the interface.

Using a pure imaginary k_{z2} the electric and magnetic field in medium 2(air, $z > 0$) can be given by

$$\mathbf{E}_2 = \begin{pmatrix} E_{x2} \\ 0 \\ E_{z2} \end{pmatrix} e^{i(k_{x2}x + k_{z2}z - \omega t)} \quad (161)$$

$$\mathbf{H}_2 = \begin{pmatrix} 0 \\ H_{y2} \\ 0 \end{pmatrix} e^{i(k_{x2}x + k_{z2}z - \omega t)} \quad (162)$$

Using a pure imaginary k_{z1} the electric and magnetic field in medium 1(metal, $z > 0$) can be given by

$$\mathbf{E}_1 = \begin{pmatrix} E_{x1} \\ 0 \\ E_{z1} \end{pmatrix} e^{i(k_{x1}x - k_{z1}z - \omega t)} \quad (163)$$

$$\mathbf{H}_1 = \begin{pmatrix} 0 \\ H_{y1} \\ 0 \end{pmatrix} e^{i(k_{x1}x - k_{z1}z - \omega t)} \quad (164)$$

From the Condition I, we can get

3.1 Condition I: $\mathbf{t} \cdot [\mathbf{E}_1 - \mathbf{E}_2] = 0$

$$k_{x1} = k_{x2} = k_x \quad (165)$$
$$E_{x1} = E_{x2} \quad (166)$$
$$E_{z1} = E_{z2} \quad (167)$$

From condition IV,

3.4 Condition IV: $\mathbf{t} \cdot [\mathbf{H}_1 - \mathbf{H}_2] = \mathbf{J}_s$

$$H_{y1} = H_{y2} \quad (168)$$
here we assume $(J_s)_y \approx 0$ (169)

From condition III,

3.3 Condition III: $\mathbf{n} \cdot (\mathbf{D}_1 - \mathbf{D}_2)$

$$\tilde{\epsilon}_1 \epsilon_0 E_{z1} = \tilde{\epsilon}_2 \epsilon_0 E_{z2} \quad (170)$$
here we assume $\sigma_{12}(k_x, \omega) \ll D_{1z}, D_{2z}$ (171)

From Eq.4 and $\mathbf{J} \approx 0$

$$\mathrm{rot}\mathbf{H} = \frac{\partial \mathbf{D}}{\partial t} \quad (172)$$

$$\mathrm{rot}\mathbf{H} = \begin{vmatrix} \mathbf{i} & \mathbf{j} & \mathbf{k} \\ \frac{\partial}{\partial x} & \frac{\partial}{\partial y} & \frac{\partial}{\partial z} \\ 0 & H_{yi} & 0 \end{vmatrix} = -\mathbf{i}\frac{\partial}{\partial z}H_{yi} + \mathbf{k}\frac{\partial}{\partial x}H_{yi} \quad (173)$$

From the $\mathbf{i}$ component of the above equation,

$$ik_{z1}H_{y1} = -i\omega\epsilon_0\tilde{\epsilon}_1 E_{x1} \quad (174)$$
$$-ik_{z2}H_{y2} = -i\omega\epsilon_0\tilde{\epsilon}_2 E_{x2} \quad (175)$$

$E_{x1} = E_{x2}$ then

$$\frac{k_{z1}}{\omega\epsilon_0\tilde{\epsilon}_1}H_{y1} + \frac{k_{z2}}{\omega\epsilon_0\tilde{\epsilon}_2}H_{y2} = 0 \quad (176)$$

$H_{y1} = H_{y2}$ then

$$\frac{k_{z1}}{\tilde{\epsilon}_1} + \frac{k_{z2}}{\tilde{\epsilon}_2} = 0 \quad (177)$$

From Eqs.(21) and (26)

$$k^2 = k_x^2 + k_{zi}^2 = \tilde{\epsilon}_i \left(\frac{\omega}{c}\right)^2 \quad (178)$$

$$k_x^2 = \tilde{\epsilon}_1 \left(\frac{\omega}{c}\right)^2 - k_{z1}^2 \quad (179)$$

$$k_x^2 = \tilde{\epsilon}_2 \left(\frac{\omega}{c}\right)^2 - k_{z2}^2 = \tilde{\epsilon}_2 \left(\frac{\omega}{c}\right)^2 - \left(-\frac{\tilde{\epsilon}_2}{\tilde{\epsilon}_1}k_{z1}\right)^2 \quad (180)$$

From the last two equations Eqs.(179) and (180).

$$k_x^2 = \left(\frac{\tilde{\epsilon}_1\tilde{\epsilon}_2}{\tilde{\epsilon}_1 + \tilde{\epsilon}_2}\right)\left(\frac{\omega}{c}\right)^2 \quad (181)$$

$$k_{z1}^2 = \left(\frac{\tilde{\epsilon}_1^2}{\tilde{\epsilon}_1 + \tilde{\epsilon}_2}\right)\left(\frac{\omega}{c}\right)^2 \quad (182)$$

$$k_{z2}^2 = \left(\frac{\tilde{\epsilon}_2^2}{\tilde{\epsilon}_1 + \tilde{\epsilon}_2}\right)\left(\frac{\omega}{c}\right)^2 \quad (183)$$

Surface plasmons II

If we remind that $\tilde{\epsilon}_1 = \epsilon_1' + i\epsilon_1''$, $\tilde{\epsilon}_2 = \epsilon_2$

$$k_x^2 = \left(\frac{\omega}{c}\right)^2 \frac{(\epsilon_1' + i\epsilon_1'')\epsilon_2}{(\epsilon_1' + i\epsilon_1'') + \epsilon_2}$$
$$= \left(\frac{\omega}{c}\right)^2 \epsilon_2 \frac{\epsilon_1'(\epsilon_1' + \epsilon_2) + \epsilon_1''^2 + i[\epsilon_1''(\epsilon_1' + \epsilon_2) - \epsilon_1' \epsilon_1'']}{(\epsilon_1' + \epsilon_2)^2 + \epsilon_1''^2} \quad (184)$$

If we assume $\epsilon_1'' < |\epsilon_1'|$

$$\mathrm{Re}(k_x) = \frac{\omega}{c}\left(\frac{\epsilon_1'\epsilon_2}{\epsilon_1' + \epsilon_2}\right)^{1/2} \quad (185)$$

$$\mathrm{Im}(k_x) = \frac{\omega}{c}\left(\frac{\epsilon_1'\epsilon_2}{\epsilon_1' + \epsilon_2}\right)^{3/2} \frac{\epsilon_1''}{2\epsilon_1'^2} \quad (186)$$

The surface plasmon decay in x-direction can be evaluated from $\mathrm{Im}(k_x)$ because the intensity decreased as $\exp[-2\mathrm{Im}(k_x)x]$. The decay length L_{12} may be obtained as

$$L_{12} = [2\mathrm{Im}(k_x)]^{-1} = \frac{c}{\omega}\left(\frac{\epsilon_1'\epsilon_2}{\epsilon_1' + \epsilon_2}\right)^{-3/2} \frac{\epsilon_1'^2}{\epsilon_1''} \quad (187)$$

For the water|metal interface the decay lengths L_{12} are 6.4 μm for gold (16.6 μm for air|gold surface), 12.3 μm for silver, and 5.5 μm for aluminum. The decay length L_{12} is the key parameter to carry out a SPR imaging measurements [11]. In addition there is a temporal decay in ω, please refer the Raether's book for details[1].

The dispersion relation k_x vs ω become close to the light line $\sqrt{\epsilon_2}\omega/c$ at small k_x, because in the limit that $\omega \to 0, \epsilon_1' >> \epsilon_2$. At large k_x the denominator of Eq.(185) becomes zero

$$\epsilon_1' + \epsilon_2 = 0 \quad (188)$$

For simple metals the dielectric constant is given by the plasma frequency ω_p[16] [12]

$$\epsilon_1' = 1 - \frac{\omega_p^2}{\omega^2} \quad (189)$$

From Eqs.(188) and (189) the surface plasma frequency ω_{sp} may be obtained as

$$\omega_{sp} = \omega_p \frac{1}{\sqrt{1 + \epsilon_2}} \quad (190)$$

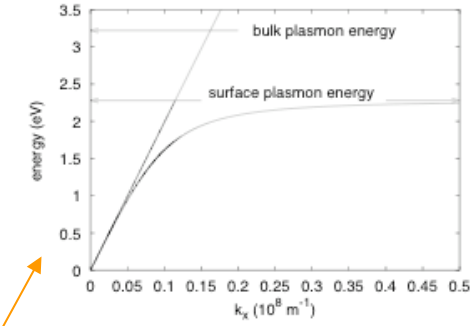

Figure 10: Surface plasmon dispersion $\omega(k_x)$ on gold surface. The vertical axis is scaled as $\hbar\omega$ (eV). The straight solid line in the figure shows the light line $k_x = \sqrt{\epsilon_2}\omega/c$. The energy of bulk plasmon is 3.22 eV, and that of surface plasmon is 2.28 eV and shown as the arrows in the figure.

Resonance conditions are evident in the dispersion curve:
group velocity → 0 around resonance
(propagation of plasmon oscillations can be achieved on relatively long range)

Maxwell eqs + boundary conditions → resonance occurrence

Surface plasmons III

Dr. Juen-Kai Wang

$$V_{k\omega}(\mathbf{r},t)=\frac{2\pi\sigma_{k\omega}}{k}e^{-k|z|}e^{i(kx-\omega t)}$$ Surface potential due to surface charge $\sigma_{k\omega}$

$$\varepsilon_1(\omega)E_z\left(z=0^+,\omega\right)=\varepsilon_2(\omega)E_z\left(z=0^-,\omega\right)$$ Boundary condition

$$\because\quad E_z\left(z=0^+,\omega\right)=-E_z\left(z=0^-,\omega\right)$$

$$\therefore\quad \boxed{\varepsilon_1(\omega)=-\varepsilon_2(\omega)}$$

Plasmon resonance condition

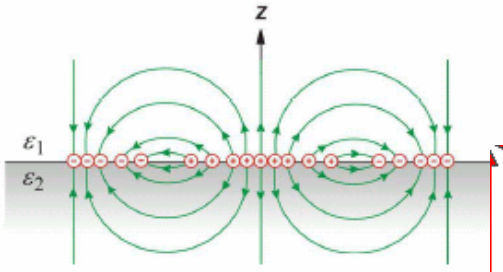

R. H. Ritchie, Phys. Rev. 106, 874 (1957).
Surface Polaritons, edited by V. M. Agranovich and D. L. Mills (North-Holland, Amsterdam, 1982).
M. G. Cottam and D. R. Tilley, Introduction to Surface and Superlattice Excitations (Cambridge University Press, Cambridge,

Note: plasmons are evident with noble metals (charges should be free as more as possible, metal should be pure, without surface oxidization or similar effects)

Surface plasmon dispersion

Dr. Juen-Kai Wang

Dispersion relation

$$\boxed{k_{\parallel}^2=\frac{\omega^2}{c^2}\frac{\varepsilon_1\varepsilon_2}{\varepsilon_1+\varepsilon_2}}$$

$$\because\quad \varepsilon_1\varepsilon_2<0 \quad\text{and}\quad k_{\parallel}^2>0$$

$$\therefore\quad \boxed{\varepsilon_1+\varepsilon_2<0}$$

For vacuum-metal surfaces,

$$\varepsilon_1=1 \qquad \varepsilon_2=1-\frac{\omega_p^2}{\omega^2}$$

$$\therefore\quad \boxed{\begin{array}{l}0<\omega<\omega_{sp}\\ \omega_{sp}^2=\dfrac{\omega_p^2}{2}\end{array}}$$

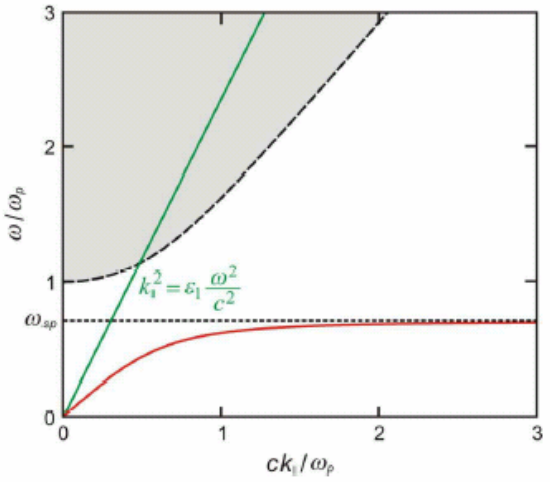

Summarizing:

✓plasmon oscillations can be seen as space and time modulations of free charges at the surface of the metal/dielectric interface

✓a resonance frequency exists (depending on material properties) where oscillation effects are enhanced

✓plasmons exhibit a longitudinal character

Surface plasmons IV

$$\because \quad k_{\parallel}^2 = \frac{\omega^2}{c^2}\frac{\varepsilon_1\varepsilon_2}{\varepsilon_1+\varepsilon_2} > \varepsilon_1\frac{\omega^2}{c^2}$$

$\therefore$ **Surface plasmon cannot be excited by a light beam incident in the normal way in medium 1.**

Raether-Kretschmann configuration

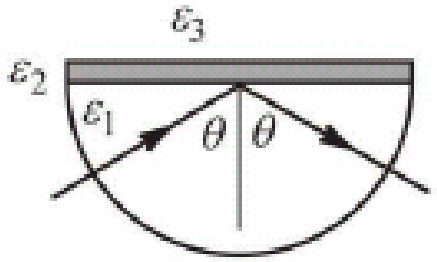

Excitation condition for surface plasmon at the 2/3 interface.

$$k_{\parallel} = \varepsilon_1^{1/2}\frac{\omega}{c}\sin\theta > \varepsilon_3^{1/2}\frac{\omega}{c}$$

Plasmon resonances can occur at a metal surface ($\varepsilon < 1$) sorrounded by a dielectric ($\varepsilon \geq 1$)

- ✓ Geometry is “anisotropic” (the plane interface layer is palying a role)
- ✓ “Electron density” waves develop along the interface layer

⇩

Surface plasmon excitation requires **longitudinal waves**

Surface plasmons can be seen only if non-conventional excitation (e.g., evanescent waves) is used

Surface plasmons are frequently exploited in a variety of applications, including highly-sensitive spectroscopy methods

Surface plasmons and nanoparticles

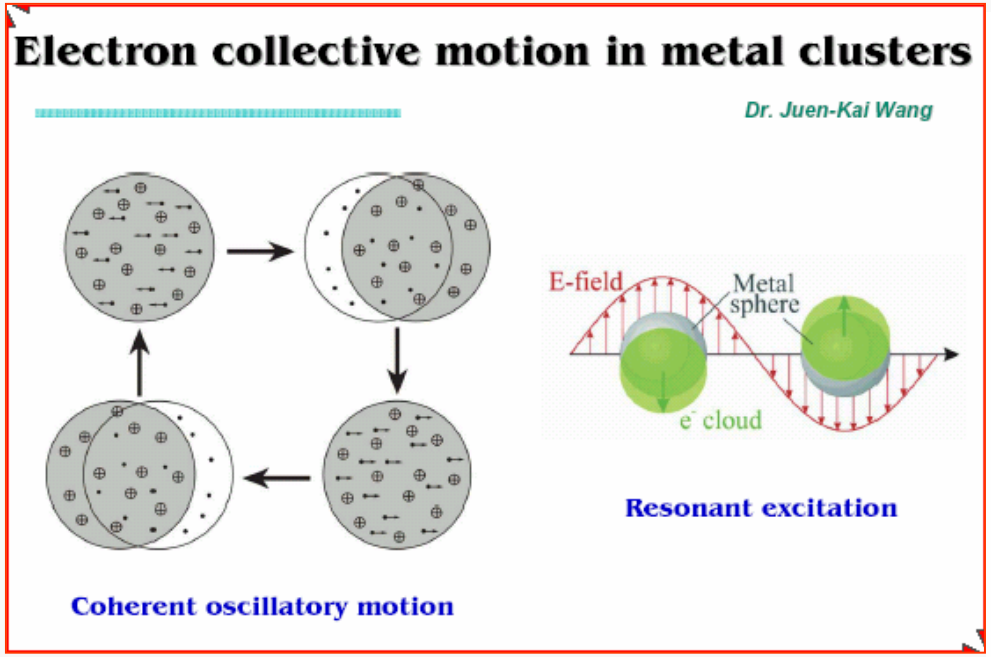

- ✓ Geometrical restrictions are relaxed (the interface layer gets a spherical shape, in case of a spherical nanoparticle)
- ✓ Excitation can be achieved with conventional (propagating) waves
- ✓ Collective plasma oscillations occur, with a “coherent” character if particle size is smaller than the wavelength

The resonant electromagnetic behavior of noble-metal nanoparticles is due to the confinement of the conduction electrons to the small particle volume. For particles with a diameter $d \ll \lambda$, the conduction electrons inside the particle move all in phase upon plane-wave excitation with radiation of wavelength λ, leading to the buildup of polarization charges on the particle surface. These charges act as an effective restoring force, allowing for a resonance to occur at a specific frequency—the particle dipole plasmon frequency-, where the response of the electrons shows a $\pi/2$ phase lag with respect to the driving field. Thus, a resonantly enhanced field builds up inside the particle, which in the small particle limit is homogeneous throughout its volume, producing a dipolar field outside the particle. This leads to enhanced absorption and scattering cross sections for electromagnetic waves, as well as to a strongly enhanced near field in the immediate vicinity of the particle surface. It is this resonantly enhanced near field from which most of the promising applications of metal nanoparticles stem. For larger particles, the spectral response is modified due to retardation effects and the excitation of higher-order (quadrupole and higher) modes, the spectral signature of which can be calculated by retaining higher orders of the Mie theory scattering coefficients.[1]

JOURNAL OF APPLIED PHYSICS 98, 011101 (2005)

APPLIED PHYSICS REVIEWS–FOCUSED REVIEW

Plasmonics: Localization and guiding of electromagnetic energy in metal/dielectric structures

Stefan A. Maier[a] and Harry A. Atwater

http://scienceworld.wolfram.com/physics/MieScattering.html

Reminders of Mie scattering

Scattering by spherical particles. This is the simplest type of scattering, since two of the scattering coefficient must identically equal zero due to symmetry. The formal rigorous solution is usually attributed to Gustav Mie (1908). Although the solution to the sphere problem appears to been attained previously, Mie was the first to *publish* it. A discussion of the history of scattering from a sphere is given by Kerker (1969).

The Mie scattering solution begins with the macroscopic Maxwell equations. Using the complex representation of the electric field **E** and auxiliary magnetic field **H**, the Maxwell equations assume the form

$$\nabla \cdot \mathbf{E} = 0 \quad (1)$$

$$\nabla \cdot \mathbf{H} = 0 \quad (2)$$

$$\nabla \times \mathbf{E} = i\omega\mu\mathbf{H} \quad (3)$$

$$\nabla \times \mathbf{H} = -i\omega\epsilon\mathbf{E} \quad (4)$$

Defining

$$k^2 \equiv \omega^2\epsilon\mu, \quad (5)$$

the vector wave equations become

$$\nabla^2\mathbf{E} + k^2\mathbf{E} = 0 \quad (6)$$

$$\nabla^2\mathbf{H} + k^2\mathbf{H} = 0. \quad (7)$$

The next step is to define a scalar function ψ from which two vectors **M** and **N** can be constructed by appropriate application of vector derivatives. In turns out that the function ψ and two vectors can be defined in such a way that, if ψ is a solution to the scalar wave equation, **M** and **N** are also solutions of the same vector wave equation. Furthermore, when defined appropriately, **M** and **N** also satisfy the requirements for electromagnetic fields. They are therefore called vector spherical harmonics by analogy with the (scalar) spherical harmonics encountered throughout mathematical physics.

It is a straightforward exercise to obtain the solution to the scalar wave equation. Since the particle is assumed to have spherical symmetry, spherical coordinates are the obvious choice for the coordinate system in which to express ∇^2. Incidentally, it is evident that the scattering problem for other particle shapes could conceivably be solved by, at this juncture, choosing a coordinate system in which the particle shape assumed a particularly simple form. Returning now to the spherical problem, a straightforward separation of variables in the spherical wave equation immediately yields a general solution

$$\psi = \sum_{l=0}^{\infty}\sum_{m=-l}^{l}[A_l^m\cos(m\phi)P_l^m(\cos\theta)z_n(kr) + B_l^m\sin(m\phi)P_l^m(\cos\theta)z_n(kr)], \quad (8)$$

where $P_l^m(x)$ are associated Legendre polynomials and $z_n(x)$ are spherical Bessel functions. This infinite series still does not solve the problem, however. The difficulty is that the boundary conditions are specified in spherical coordinates (in keeping with the symmetry of the particle), but the incident wave is planar and is still given in Cartesian coordinates. In order to express the incident wave and boundary conditions in the same coordinate system, it is therefore necessary to either expand the plane wave in vector spherical harmonics, or the sphere boundary conditions in appropriate Cartesian coordinates. The conventional although by no means trivial approach is to expand the plane wave in vector spherical harmonics. The calculus becomes quite involved, so only the solution will be quoted here. The desired expansion of the complex plane wave (denoted $\mathbf{E}_c$) in terms of spherical harmonics turns out to be given by

$$\mathbf{E}_c = \sum_{m=-l}^{l}\sum_{n=0}^{\infty}(B_{mn}^e\mathbf{M}_{mn}^e + B_{mn}^o\mathbf{M}_{mn}^o + A_{mn}^e\mathbf{N}_{mn}^e + A_{mn}^o\mathbf{N}_{mn}^o). \quad (9)$$

If the plane wave is polarized in the x-direction and moving along the z-axis, then only $m = 1$ contributes, so the expansion becomes

$$\mathbf{E}_c = \sum_{n=0}^{\infty} i^n\frac{2n+1}{n(n+1)}[\mathbf{M}_{1n}^{o\,(1)} - i\mathbf{N}_{1n}^{e\,(1)}]. \quad (10)$$

The combination of vector spherical harmonics occurring in this expansion can be split into two scalar components, each of which contains a spherical Bessel function of the first kind. The initial field outside the sphere is now known.

Two additional fields must be computed: the scattered wave outside the sphere, and the wave produced inside the sphere itself. Both are similar to the expansion of the incident wave in form, but the scattered wave outside the sphere involves spherical Hankel functions of the first kind, while that inside involves spherical Bessel functions of the first kind. The reason for this apparent asymmetry is readily explained. The Hankel functions are linear combinations of the Bessel functions of the first kind, which are singular at infinity, and Bessel functions of the second kind (also known as Weber or Neumann functions), which are singular at the origin. It is because of the Bessel function of the second kinds' unphysical singularity at the origin that the interior wave must be composed only of Bessel functions of the first kind.

The boundary conditions require that the transverse components of the total electric and magnetic fields (equal to the sum of incident and scattered fields minus the interior field) equal zero at the surface. The fields determined above are now inserted into the boundary conditions, and four expressions obtained, one for each component of the internal and scattered fields. However, if the permeability of the particle and medium are identical, then the four expressions reduce to only two. The series of constants obtained are denoted a_n and b_n. These expressions, in slightly simplified form, are given by

Goody and Yung (1989). By defining supplementary functions $\pi_n(x)$ and $\tau_n(x)$, the **E** and **H** fields may be expressed in reasonably concise form. From these expressions, the amplitude functions S_1 and S_2 are finally obtained

$$S_1(\theta) = \sum_{n=1}^{\infty}\frac{2n+1}{n(n+1)}[a_n\pi_n(\cos\theta) + b_n\tau_n(\cos\theta)] \quad (11)$$

(12)

$$S_2(\theta) = \sum_{n=1}^{\infty}\frac{2n+1}{n(n+1)}[b_n\pi_n(\cos\theta) + a_n\tau_n(\cos\theta)]. \quad (13)$$

The form of extinction and scattering efficiencies is even simpler. The series for **E** and **H** which were used to the scattering amplitude functions may be inserted into the appropriate integrals, and the integration carried out term by term. The results of this exercise are

$$Q_{\text{ext}} = \frac{2}{x^2}\sum_{n=1}^{\infty}(2n+1)\Re(a_n + b_n) \quad (14)$$

$$Q_{\text{sca}} = \frac{2}{x^2}\sum_{n=1}^{\infty}(2n+1)(|a_n|^2 + |b_n|^2), \quad (15)$$

where equation (15) is the correct form of Goody and Yung's (1989) erroneous equation (7.67a). The effort required to obtain these solutions was substantial indeed. However, an analytical solution to the scattering problem is now known. Unfortunately, the infinite series which must be evaluated exhibits inconveniently slow convergence. In fact, to obtain accurate results for a sphere with a size factor

$$x \equiv \frac{2\pi a}{\lambda}, \quad (16)$$

approximately x terms must be evaluated. Practical evaluation of these series must therefore be undertaken with the aid of computers. Even then, however, a calculation using the Mie theory as currently formulated becomes less and less practical for $r \gg \lambda$.

For purely spherical particles, an **analytical solution** exists describing the scattering cross-section (derived in terms of Bessel and Legendre functions)

Accuracy is larger for smaller size particles

Mie scattering and metal nanoparticles

Mie scattering: elastic process with an isotropic ("dipole-like") character and rather independent of wavelength (contrary to Rayleigh)

(Frequently used to describe atmosphere scattering events, as a competitive process with respect to Rayleigh)

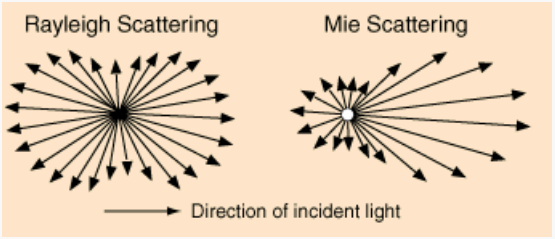

Experimentalists typically measure particle extinction. Extinction is absorption plus scattering. Scattering arises when charged particles are accelerated by a field and reradiate. Absorption occurs when the particle takes energy out of the beam and converts it to other forms. Extinction is the sum of both of these processes. The Mie Theory expression for extinction efficiency is

$$Q_{ext} = \frac{2}{(kr)^2}\sum_{n=1}^{\infty}(2n+1)\mathrm{Re}\{a_n + b_n\},$$

(2)

where $k = 2\pi/\lambda$ (wavenumber), r is the sphere radius, and a and b are the expansion coefficients of the scattered field.

For small particles, only the first term(s) of the expansion must be retained!

This corresponds to a "quasi-static" approximation, that is retardation effects can be beglected, i.e., electrons do follow almost completely the driving force

Effective medium polarization (i.e., dielectric constant) must be considered, as seen with layers and surface plasmons

For a spherical metal nanoparticle of radius $a \ll \lambda$ embedded in a nonabsorbing surrounding medium of dielectric constant ε_m, the quasistatic analysis gives the following expression for the particle polarizability α:

$$\alpha = 4\pi a^3 \frac{\varepsilon - \varepsilon_m}{\varepsilon + 2\varepsilon_m}, \quad (1)$$

Clausius-Mosotti like expression!

with the complex $\varepsilon = \varepsilon(\omega)$ describing the dispersive dielectric response of the metal. The polarizability and thus the induced homogeneous polarization inside the particle are resonantly enhanced at the Fröhlich frequency where the denominator shows a minimum, limited by the imaginary part of ε describing Ohmic heating losses within the particle.

Maier, Atwater, JAP (2005)

Mie scattering II

Although a number of theoretical models have been proposed (Kelly et al., 2003), the original classical model of Mie (Born and Wolf, 1998) is often used to describe the optical properties of the metal nanoparticles. Often one utilizes a dipole approximation in which the oscillation of conduction electrons (plasmon oscillations), driven by the electromagnetic field of light, produces oscillating dipoles along the field direction where the electrons are driven to the surface of the nanoparticles as shown in Figure 5.3. A more rigorous theory (Kelly et al., 2003) shows that this dipolar-type displacement is applicable to smaller-size particles and gives rise to an extinction coefficient k_{ex} (measure of absorption and scattering strengths collectively) by the following equation (Kreibig and Vollmer, 1995):

$$k_{ex} = \frac{18\pi N V \varepsilon_h^{3/2}}{\lambda} \frac{\varepsilon_2}{[\varepsilon_2 + 2\varepsilon_h]^2 + \varepsilon_2^2} \qquad (5.1)$$

Here λ is the wavelength of light, and ε_h is the dielectric constant of the surrounding medium. The terms ε_1 and ε_2 represent the real and the imaginary parts of the dielectric constant, ε_m, of the metal ($\varepsilon_m = \varepsilon_1 + i\varepsilon_2$) and are dependent on the frequency ω of light. If ε_2 is small or weakly dependent on ω, the absorption maximum corresponding to the resonance condition is produced when $\varepsilon_1 = -2\varepsilon_h$, leading to a vanishing denominator. Hence, a surface plasmon resonance absorption is produced at optical frequency ω at which the resonance condition $\varepsilon_1 = -2\varepsilon_h$ is fulfilled. The size dependence of the surface plasmon resonance comes from the size dependence of the dielectric constant ε of the metal. This is often described as the intrinsic size effect (Link and El-Sayed, 2003). In the case of noble metals such as gold, there are two types of contributions to the dielectric constant of the metal: One is from the inner *d* electrons, which describes interband transition (from inner *d* orbitals to the conduction band), and the other is from the free conduction electrons. The latter contribution, described by the Drude model (Born and Wolf, 1998; Kreibig and Vollmer, 1995), is given as

$$\varepsilon_D(\omega) = 1 - \frac{\omega_p^2}{\omega^2 + i\gamma\omega} \qquad (5.2)$$

where ω_p is the plasmon frequency of the bulk metal and γ is the damping constant relating to the width of the plasmon resonance band. It relates to the lifetime associated with the electron scattering from various processes. In the bulk metal, γ has main contributions from electron–electron scattering and electron–phonon scattering, but in small nanoparticles, scattering of electrons from the particle's boundaries (surfaces) becomes important. This scattering produces a damping term γ that is inversely proportional to the particle radius *r*. This dependence of γ on the particle size introduces the size dependence in $\varepsilon_D(\omega)$ [thus ε_1 in Eq. (5.1)] and, consequently, in the surface plasmon resonance condition.

For larger-size nanoparticles (>25 nm for gold particles), higher-order (such as quadrupolar) charge cloud distortion of conduction electrons becomes important, as shown in Figure 5.4. These contributions induce an even more pronounced shift of the plasmon resonance condition as the particle size increases. This effect for the larger size particle is referred to as the *extrinsic size effect* (Link and El-Sayed, 2003). The position and the shape of the plasmon absorption band also depends on the dielectric constant ε_h of the surrounding medium as the resonance condition is described by $\varepsilon_1 = -2\varepsilon_h$ (see above). Hence, an increase in ε_h leads to an increase in the plasmon band intensity and band width, as well as produces a red shift of the plasmon band maximum (Kreibig and Vollmer, 1995). This effect of enhancing the plasmon absorption by using a higher dielectric constant surrounding medium

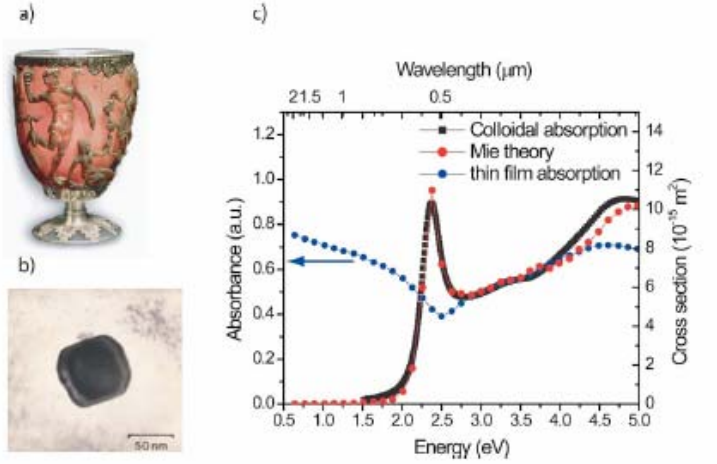

FIG. 1. (Color online) (a) The Lycurgus glass cup, demonstrating the bright red color of gold nanocrystals in transmitted light. (b) scanning electron microscopy (SEM) image of a typical nanocrystal embedded in the glass (courtesy of the British museum). (c) Calculated absorption spectrum of a thin gold film (blue dots) and of 30-nm Au nanoparticles in water (red dots) using classical electromagnetic theory. A measured absorption spectrum of an aqueous solution of 30-nm Au colloids (black dots) shows good agreement with the theory.

Calculations based on Mie scattering and accounting for the effective dielectric constant do fit well the observations

Optical behavior of metal nanoparticles II

In comparison to the semiconductor nanoparticles where quantum confinement produces quantization of the electron and hole energy states to produce major modifications of their optical spectra, metallic nanoparticles exhibit major changes in their optical spectra derived from effects that can be explained using a classical dielectric picture. The light absorption by metallic nanoparticles is described by coherent oscillation of the electrons, which is induced by interaction with the electromagnetic field. These oscillations produce surface plasmon waves. It should be noted that the term "surface plasmons" is used to describe the excitations at the metal–dielectric interface in the case of flat surfaces, where the plasmons can only be excited by using special geometries (e.g., the Kretschmann geometry as described in Chapter 2) required for matching of the wavevector, k_{sp}, of the surface plasmon wave with that of light producing it. In the case of metal nanostructures (e.g., nanoparticles), plasmon oscillations are localized and thus not characterized by a wavevector k_{sp}. To make a distinction, the plasmon modes in metallic nanoparticles are also sometimes referred to as localized surface plasmons. These localized plasmons are excited by light absorption in the nanoparticles, with the specific absorption bands being referred to as *plasmon bands*. To excite these localized plasmons in metallic nanostructures, no special geometry, such as those required for plasmon excitation along a planar metal–dielectric interface, is required. The specific wavelengths of light absorption producing plasmon oscillations are called surface plasmon bands or simply plasmon bands.

The main photonic applications of the metallic nanoparticles are derived from the local field enhancement under the resonance plasmon generation condition, which leads to enhancement of various light-induced linear and nonlinear optical processes within nanoscopic volume of the media surrounding the nanoparticles. Such field enhancement has been used for apertureless near-field microscopy. Another application presented by the metallic nanoparticles is that using an array of interacting metallic nanoparticles; light can be coupled and propagated as an electromagnetic wave through a dimension of nanometers in cross section, much smaller than the optical waveguiding dimension.

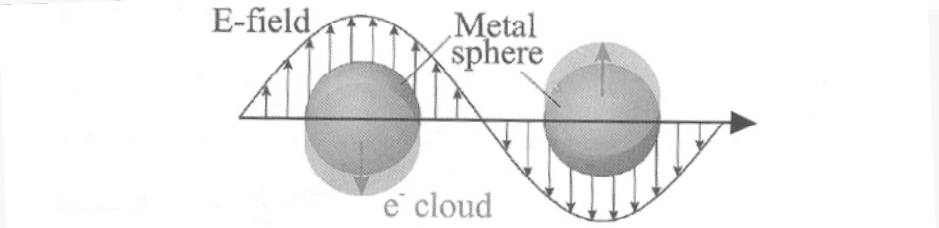

Figure 5.3. Schematic of plasmon oscillation in a metal nanosphere. From Kelly et al. (2003), reproduced with permission.

- For metallic nanoparticles significantly smaller than the wavelength of light, light absorption is within a narrow wavelength range. The wavelength of the absorption peak maximum due to the surface plasmon absorption band is dependent on the size and the shape of the nanocrystals, as well as on the dielectric environment surrounding the particles.
- For extremely small particles (<25 nm for gold), the shift of the surface plasmon band peak position is rather small. However, a broadening of the peak is observed.
- For larger nanoparticles (>25 nm for gold), the surface plasmon peak shows a red shift. Figure 5.1 illustrates these features for a series of gold nanoparticles of different sizes.

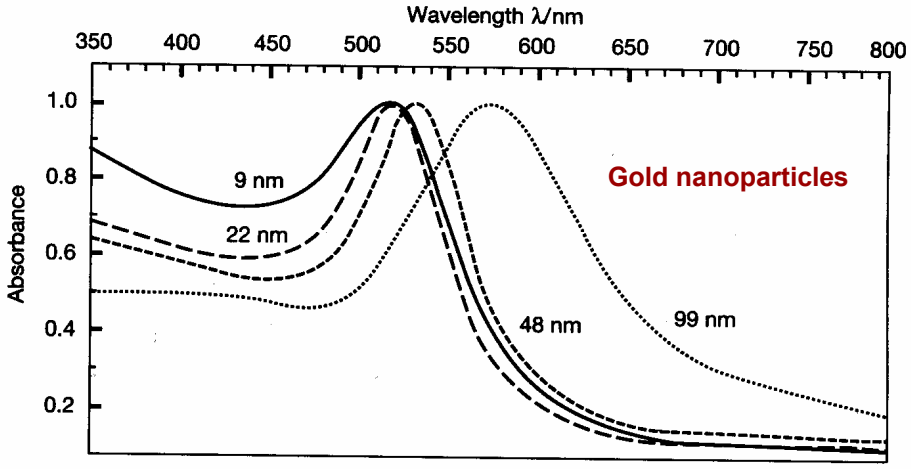

Figure 5.1. Optical absorption spectra of gold nanoparticles of different sizes. From Link and El-Sayed (1999), reproduced with permission.

Red-shift of the absorption peak observed as particle size increases

Optical behavior of metal nanoparticles III

The origin of these shifts is not due to quantum confinement. The quantum confinement does affect the energy spacing of the various levels in the conduction band. However, the quantization, derived from the confinement, affects the conductive properties of the metal and is often used to describe the metal-to-insulator transition occurring as the particle size is reduced from microscopic to nanoscopic size. When the dimensions of the metallic nanoparticles are large, the spacing of levels within the conduction band is significantly less than the thermal energy, kT (k is Boltzmann's constant and T is the temperature in kelvin), and the particle exhibits a metallic behavior. When the nanoparticles approach a size at which the increased energy separation due to the quantum confinement effect (smaller length of the box for the free electron) is more than the thermal energy, an insulating behavior results because of the presence of these discrete levels. However, the energy level separations are still too small to affect the optical properties of metals in the UV to the IR range.

Red shift observed also as a function of the environment dielectric constant

Au nanoparticle core surrounded by SiO_2 shell

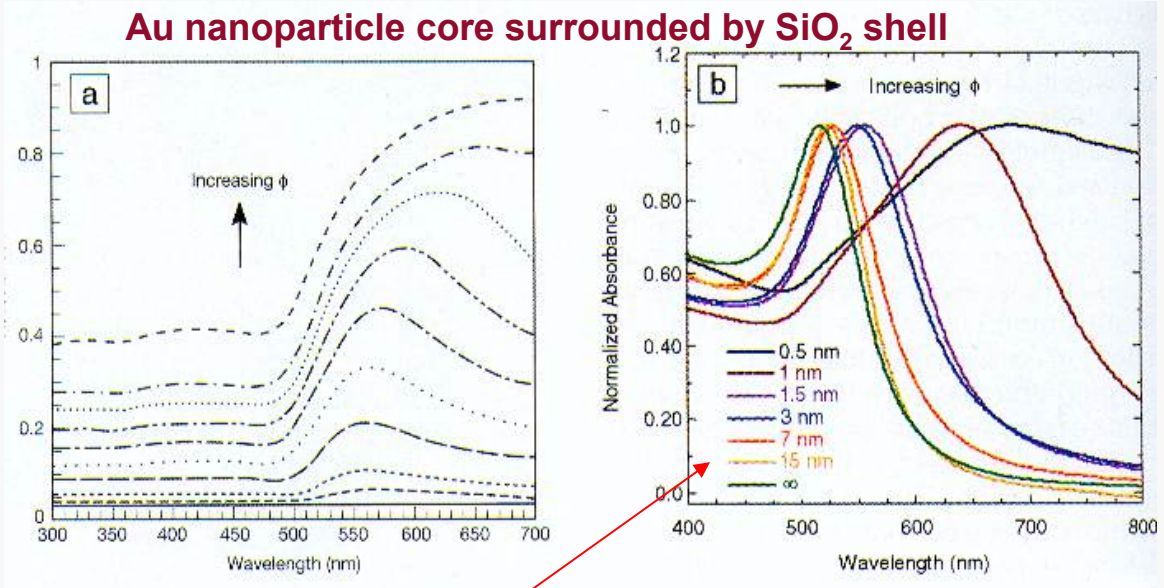

Figure 6. (a) Normalized reflectance spectra for Au@SiO_2 (gold concentrically coated by silica) films as a function of the volume fraction ϕ of Au. From the bottom curve upward, ϕ for each curve, respectively, is 0.01, 0.05, 0.10, 0.20, 0.30, 0.40, 0.50, 0.60, 0.70, and pure Au. (b) The normalized absorbance of a series of Au@SiO_2 films as a function of particle spacing.

Color depends on particle size, features of the sorrounding dielectric and interparticle spacing (collective interparticle effects!)

(Envisioned) nano-optics applications for plasmonics I

Isolated metal nanoparticles act as localized near-field sources (as already seen), with applications also in field enahncement

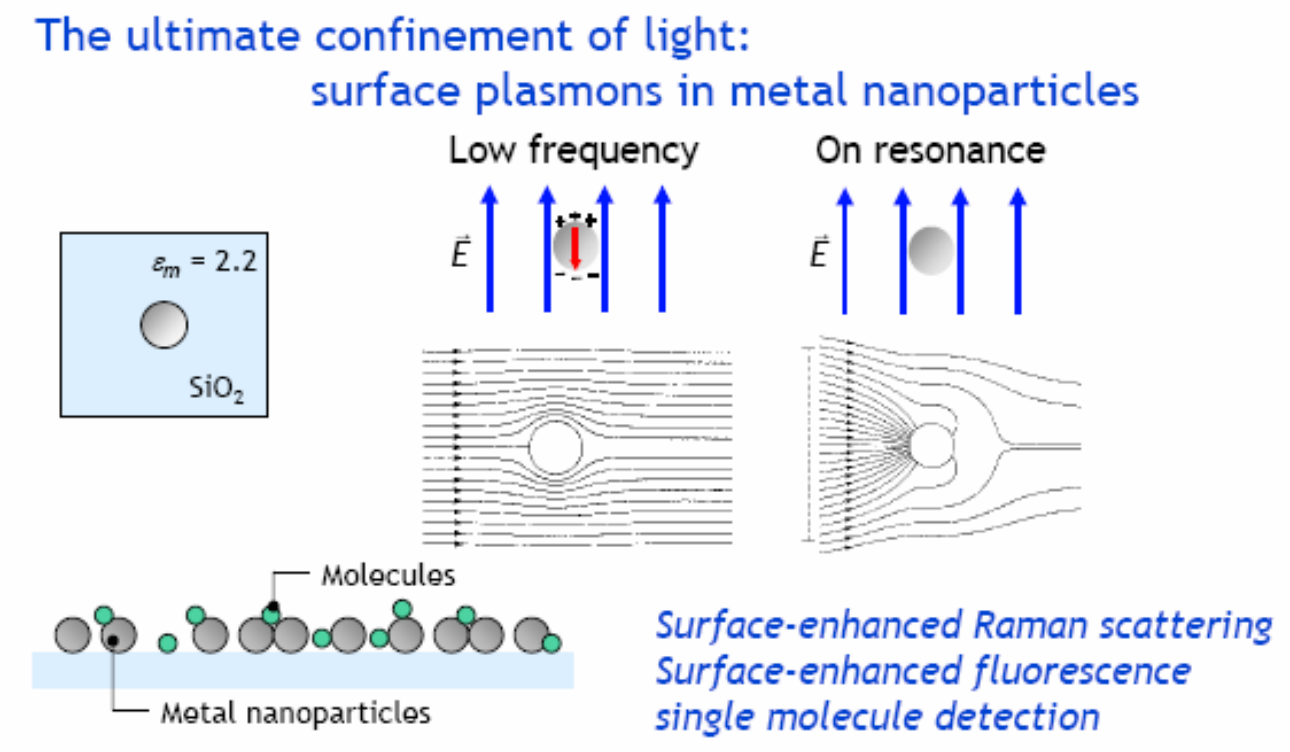

Surface plasmon nanophotonics:
optics below the diffraction limit

Albert Polman

Center for *nano*photonics
FOM-Institute AMOLF, Amsterdam

See, e.g.,

Other possible exploitations in modification/enhancement of photonics performance of various devices

(Envisioned) nano-optics applications for plasmonics II

B. Interacting particle ensembles as a basis for applications of metal nanoparticles in optical devices

Advances in particle synthesis and fabrication techniques (for example, Refs. 22, 27, and 28) have recently allowed for studies of ordered arrays of noble-metal nanoparticles. In such arrays, each nanoparticle with a diameter much smaller than the wavelength λ of the exciting light acts as an electric dipole. Thus, two types of electromagnetic interactions between the particles can be distinguished, depending on the spacing d between adjacent nanoparticles. For particle spacings on the order of the exciting wavelength λ, far-field dipolar interactions with a d^{-1} dependence dominate. Work on regular two-dimensional arrays of Au nanoparticles has indeed confirmed the existence of such interactions, and quantified their influence on both the spectral position of the collective dipolar extinction peak and the plasmon damping characteristics.[29] Figures 3(a) and 3(b) show an example of the dependence of both extinction peak and plasmon decay time on the grating constant d for a regular square array of 150-nm-diameter Au nanoparticles. Both the variation of the spectral position and width of the resonances can be explained by assuming far-field dipolar interactions—the ensemble acts effectively as a grating, leading to increased radiation damping of the collective resonances for grating constants where grating orders change from evanescent to radiative in character.[29] Applications of such ordered arrays lie, for example, in the possibility of maximizing surface-enhanced Raman scattering of adsorbed molecules by careful spectral tuning of the plasmon resonance.[30]

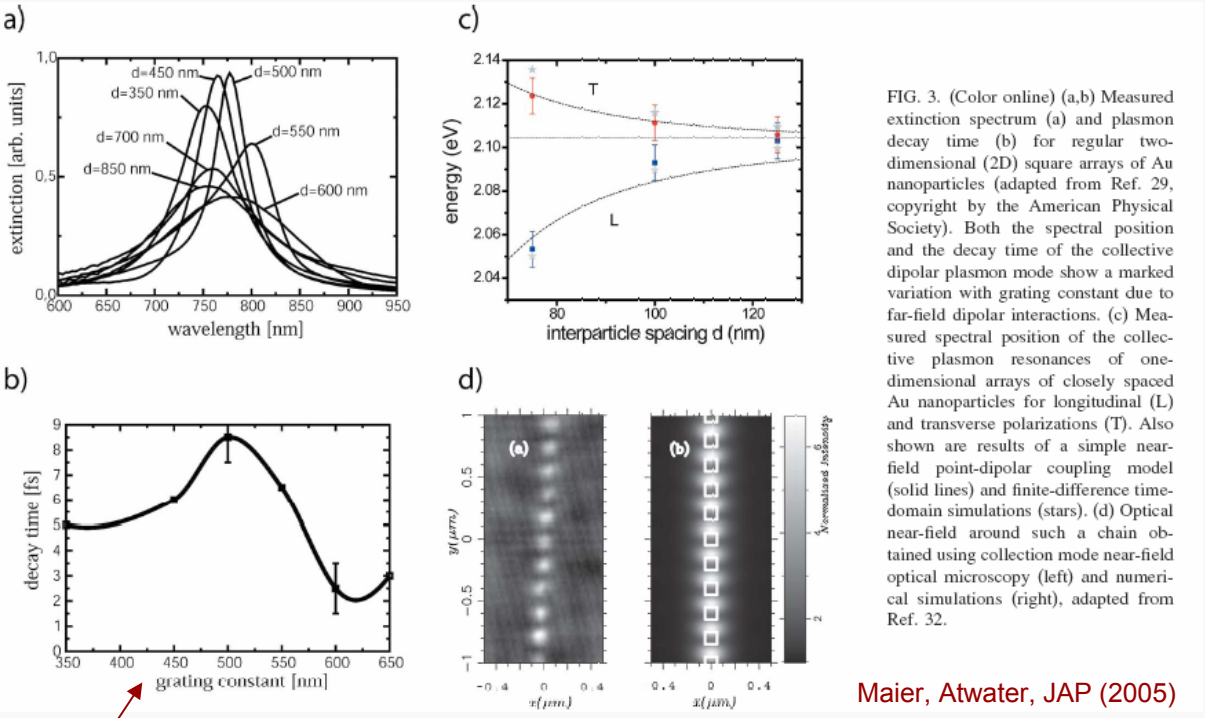

FIG. 3. (Color online) (a,b) Measured extinction spectrum (a) and plasmon decay time (b) for regular two-dimensional (2D) square arrays of Au nanoparticles (adapted from Ref. 29, copyright by the American Physical Society). Both the spectral position and the decay time of the collective dipolar plasmon mode show a marked variation with grating constant due to far-field dipolar interactions. (c) Measured spectral position of the collective plasmon resonances of one-dimensional arrays of closely spaced Au nanoparticles for longitudinal (L) and transverse polarizations (T). Also shown are results of a simple near-field point-dipolar coupling model (solid lines) and finite-difference time-domain simulations (stars). (d) Optical near-field around such a chain obtained using collection mode near-field optical microscopy (left) and numerical simulations (right), adapted from Ref. 32.

Maier, Atwater, JAP (2005)

Collective effects based on far-field interparticle interaction or near-field interparticle interaction

For particle spacings much smaller than the wavelength of light, near-field dipolar interactions between adjacent particles with a distance dependence of d^{-3} dominate.[23,31] These strongly distance-dependent interactions lead to a splitting of the plasmon dipolar peak for regular one-dimensional arrays of metal nanoparticles as seen in Fig. 3(c) for ordered arrays of 50-nm Au particles. The spectral position of the extinction peak for far-field excitation shows a blueshift for polarization perpendicular to the chain axis (T), and a redshift for longitudinal polarization (L), which can easily be understood by analyzing Coulombic force interactions between the electrons in neighboring particles. The near-field interactions between such particles have been directly visualized using near-field optical microscopy,[32] confirming a strongly enhanced field between the particles [Fig. 3(d)], indicative of near-field coupling.

One application of near-field coupling between particles in ordered arrays is the use of such structures as waveguides for electromagnetic energies at optical frequencies with a lateral mode profile below the diffraction limit of light.[6,33] Indeed, it has been shown both theoretically[34] and experimentally[35] that such arrays can guide electromagnetic energy over distances of several hundred nanometers via near-field particle interactions. Such structures could potentially be used in nanoscale all-optical networks, contributing to a class of functional optical devices below the diffraction limit of light.[5,6,36]

Guiding of light envisioned

(Envisioned) nano-optics applications for plasmonics II

Final goal: surface plasmon nanophotonic waveguides

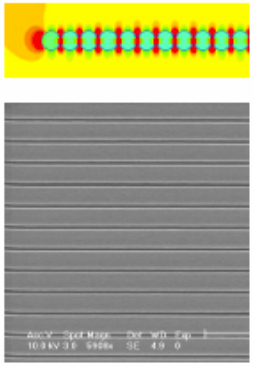

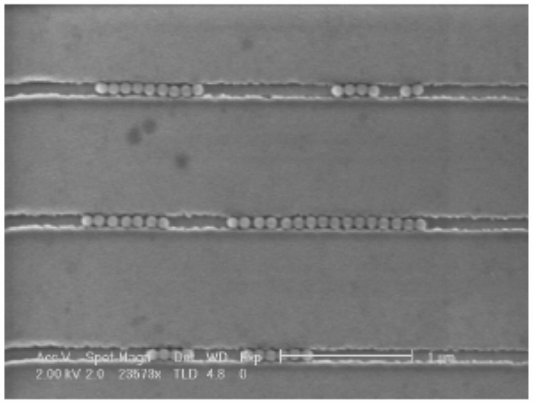

Plasmonics: energy transfer and confinement of light below the diffraction limit

Collective excitation of plasmon resonances in ordered arrays of metal nanoparticles can lead to optical guiding in a size range below the diffraction limit

~~Photonic~~ integrated circuits on silicon

Plasmonic

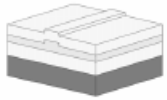

$SiO_2/\cancel{Al_2O_3}/SiO_2/Si$

Al

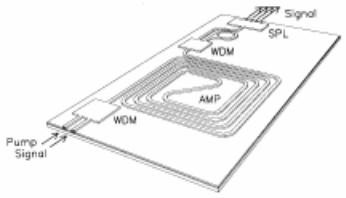

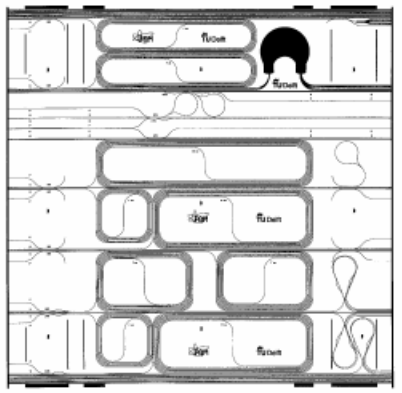

1 mm

~~10~~ µm

Opto-electronic integration, (e.g. interconnects)

Plamonic nanolithography

Plasmon waveguides can break the miniaturization limits imposed by optics (with the side advantage of integrability)

Metal nanoparticle preparation (a few words)

A huge variety of methods exists to produce (noble) metal nanoparticles *with relatively controlled shape and size* (issue well established for catalyst fabrication!)

Most of them exploits solution-based techniques leading to colloidal dispersion of nanoparticles

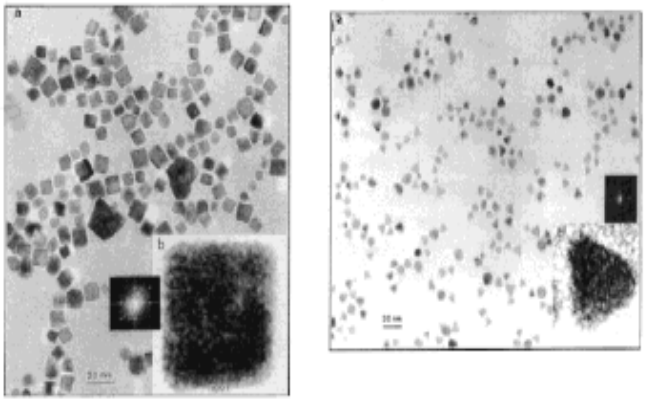

FIGURE 1. Platinum nanoparticles synthesized in colloidal solution and having different shapes (11-nm cubes on the left and ~7-nm tetrahedrons on the right).[27] The potential use of these nanoparticles for different types of catalyses drives our research interest in these particles. Do these different shapes have different catalytic properties?

For details see, e.g.,:

Some Interesting Properties of Metals Confined in Time and Nanometer Space of Different Shapes

MOSTAFA A. EL-SAYED*

VOLUME 34 NUMBER 4 ACCOUNTS of CHEMICAL RESEARCH APRIL 2001

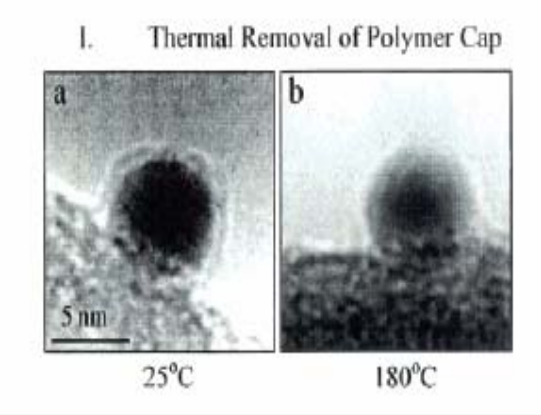

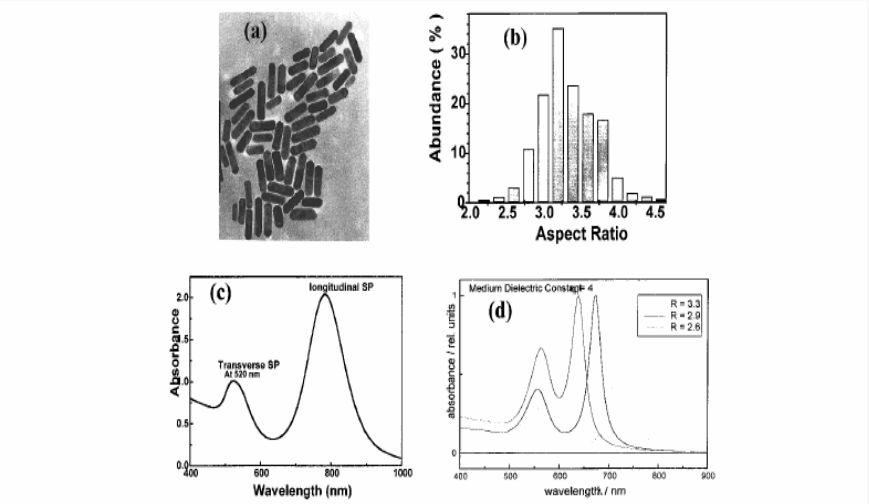

FIGURE 3. (a) TEM image of gold nanorods synthesized electrochemically in micellar solution[38] under the best conditions. (b) Size distribution of the nanorods. (c) Absorption spectrum of these nanorods. (d) Simulated spectra of nanorods of different aspect (length to width) ratios.

An example of preparation method

Materiale tratto dal seminario di M. Barnabò, Apr. 2004

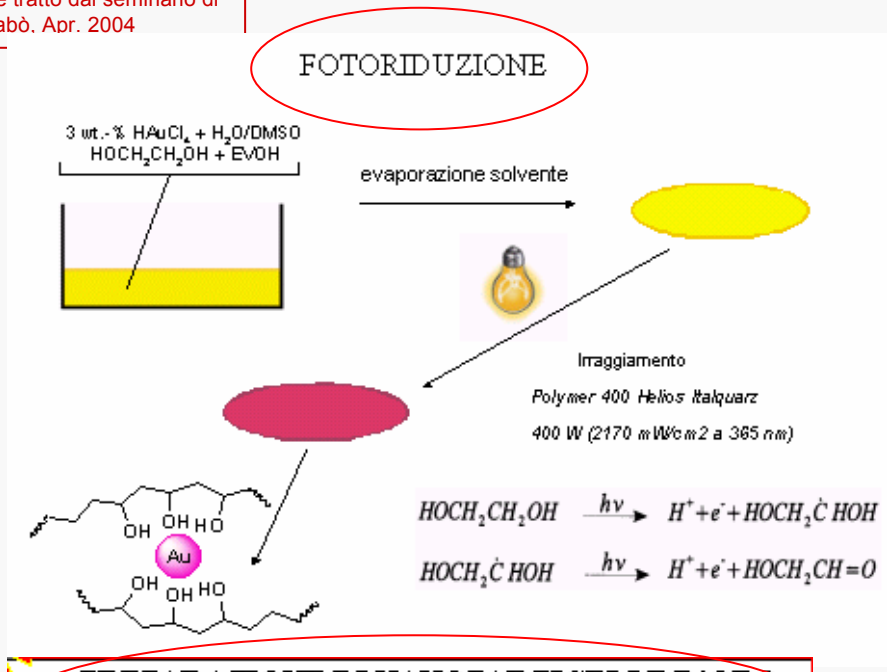

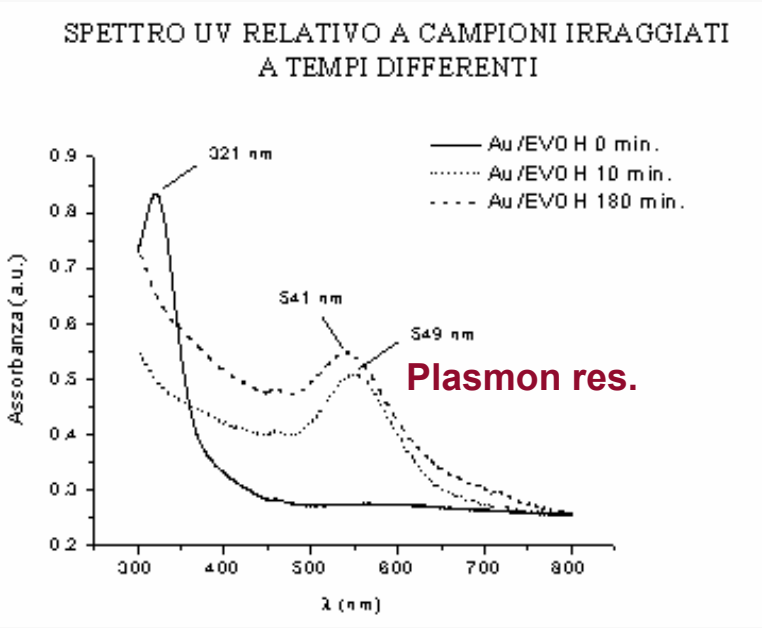

PREPARAZIONE DI NANOPARTICELLE D'ORO STABILIZZATE DA AMMINA O DA TIOLO:

$$m AuCl_{4\,(aq.)}^- + m N(C_8H_{17})_4^+{}_{(toluene)} \longrightarrow m[N(C_8H_{17})_4^+AuCl_4^-]_{(toluene)}$$

CON AMMINA

$$m[N(C_8H_{17})_4^+AuCl_4^-]_{(toluene)} + n(alchilammina)_{(toluene)} + 3me^-_{(aq.)} \longrightarrow$$

$$\longrightarrow 4mCl^-_{(aq.)} + (Au_m)(alchilammina)_{(ox)(toluene)} + x(alchilammina)_{(toluene)}$$

$$+ m[N(C_8H_{17})_4^+]_{(toluene\,aq.)}$$

CON TIOLO

$$m[N(C_8H_{17})_4^+AuCl_4^-]_{(toluene)} + nC_{12}H_{25}SH_{(toluene)} + 3me^- \longrightarrow$$

$$\longrightarrow 4mCl^-_{(aq.)} + (Au_m)(C_{12}H_{25}SH)_{n(toluene)}$$

In order to avoid undesired large-scale coalescence of metal atoms into large fragments, surfactant agents (e.g., ammines) must be used

Frequently, thiol molecules (**SAM**, we will see more on them) are used to stabilize Au nanoparticles in solution

4. An emerging technology: photonic crystals (a few words)

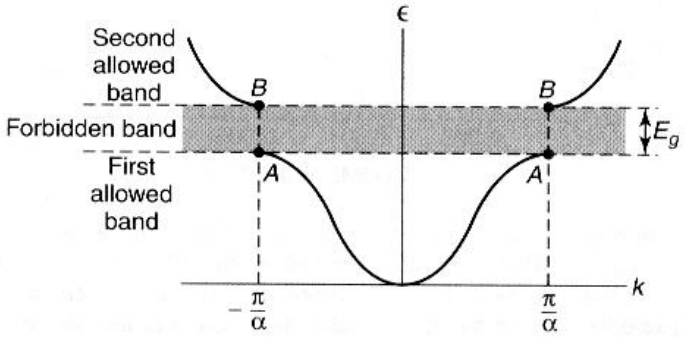

Figure 6.29. Curve of energy E plotted versus wavevector k for a one-dimensional line of atoms.

In solid-state physics:
In a crystal lattice, a periodic potential leads to the appearance of energy **gap** for the electron wavefunction

C.P.Poole F.J.Owens
Introd. to Nanotechnology
(Wiley, 2003)

important result is that there is an energy gap of width E_g, meaning that there are certain wavelengths or wavevectors that will not propagate in the lattice. This is a result of Bragg reflections. Consider a series of parallel planes in a lattice separated by a distance d containing the atoms of the lattice. The path difference between two waves reflected from adjacent planes is $2d \sin \Theta$, where Θ is the angle of incidence of the wavevector to the planes. If the path difference $2d \sin \Theta$ is a half-wavelength, the reflected waves will destructively interfere, and cannot propagate in the lattice, so there is an energy gap. This is a result of the lattice periodicity and the wave nature of the electrons.

Possible interpretation for the gap occurrence:
Bragg-like interference

Already seen in DBR:
Radiation and particles do behave similarly!!

Eq. Schroedinger --> eq. Helmoltz

$$\nabla^2 H(r) + \varepsilon\left[\frac{\omega^2}{c^2}\right] H(r) = 0$$

Photonic band gap crystals I

Equivalent crystal representations:

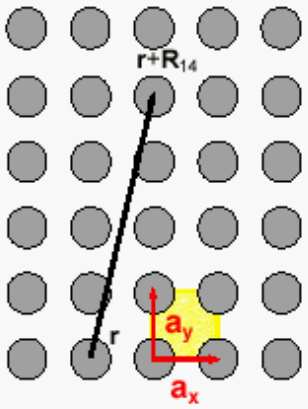

primitive lattice vectors

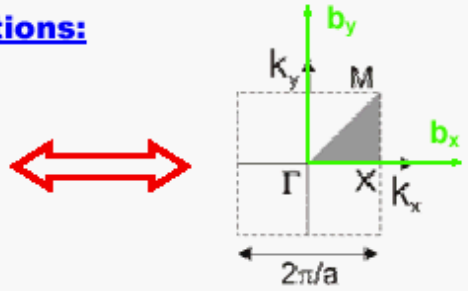

reciprocal lattice
(1st Brillouin zone)

See http://nccr-qp.epfl.ch/qpproject9.htm

$$\varepsilon(\vec{r}) = \varepsilon(\vec{r} + \vec{R}_{mn})$$
$$\vec{R}_{mn} = m \cdot \vec{a}_x + n \cdot \vec{a}_y$$

$$\Phi_k(\vec{r} + \vec{R}_{mn}) = e^{i\vec{k}\cdot\vec{R}_{mn}} \cdot \Phi_k(\vec{r})$$
$$\vec{k} \in 1^{st}\,B.Z.: \left\{\vec{b}_x, \vec{b}_y \,\middle|\, \vec{a}_i \cdot \vec{b}_j = 2\pi \cdot \delta_{ij}\right\}$$
$$\omega_k(\vec{k}) = \omega_k(\vec{k} + G_{pq})$$
$$\vec{G}_{pq} = p \cdot \vec{b}_x + q \cdot \vec{b}_y$$

Band gap crystals can be produced for radiation (photonics) by building lattices comprised of elements showing different refractive indexes

Typical size range: fraction of wavelengths (hundreds/tens of nm)

Photonic Crystals:

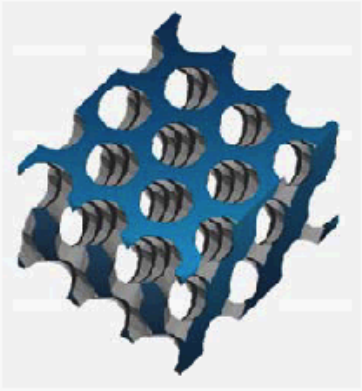

- **Strong periodic perturbation of dielectric material.**
- **Constitutes an artificial dielectric crystal structure → the photonic crysral (PC).**
- **Exhibits wavelength regimes where no propagating solutions are allowed → the photonic bandgap (PBG).**
- **Breaking of the crystal symmetry → crystal defects.**
- **Defects: Enable the appearance of localized field states.**

Photonic band gap crystals II

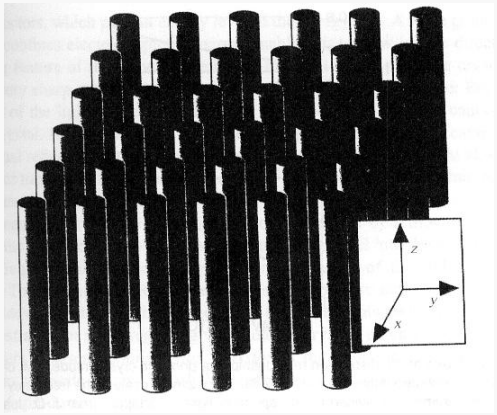

Band gap

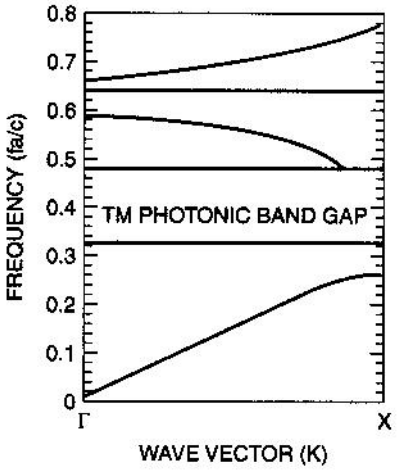

C.P.Poole F.J.Owens
Introd. to Nanotechnology
(Wiley, 2003)

Figure 6.31. A part of the dispersion relationship of a photonic crystal mode, TM, of a photonic crystal made of a square lattice of alumina rods. The ordinate scale is the frequency *f* multiplied by the lattice parameter *a* divided by the speed of light *c*. [Adapted from J. D. Joannopoulos, *Nature* **386**, 143 (1997).]

A simple 2D PC (reg. array of dielectric cylinders)

By engineering the array the band gap can be *locally* removed (or created)

Waveguiding effects

Integrated waveguides with no minimum bending angle can be created

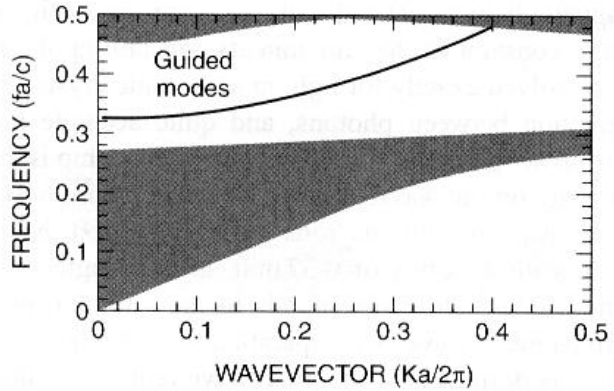

Figure 6.32. Effect of removing one row of rods from a square lattice of a photonic crystal, which introduces a level (guided mode) in the forbidden gap. The ordinate scale is the frequency *f* multiplied by the lattice parameter *a* divided by the speed of light *c*. [Adapted from J. D. Joannopoulos, *Nature* **386**, 143 (1997).]

Photonic band gap crystals III

Propagation losses are due to coupling with evanescent fields which can be observed with SNOM

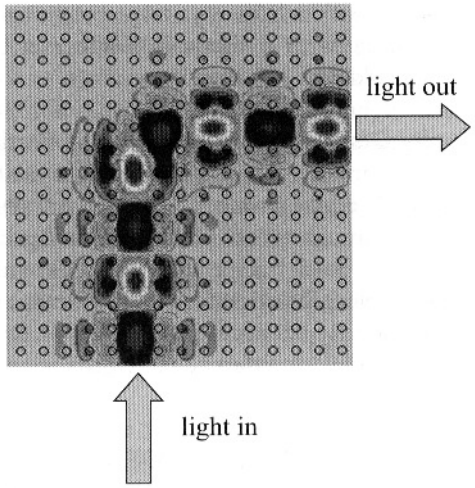

Figure 9.23. Theoretical modeling of field distribution around a defect path way, produc a sharp bend in light propagation. From Mekis et al. (1996), reproduced with permission.

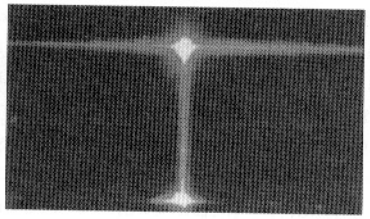

Figure 9.24. A helium–neon laser glows as it enters the waveguide at the bottom and hits the photonic crystal at the top, where it undergoes a sharp bend to propagate in the left and right directions. From Parker and Charlton (2000), reproduced with permission.

Examples of PCs I

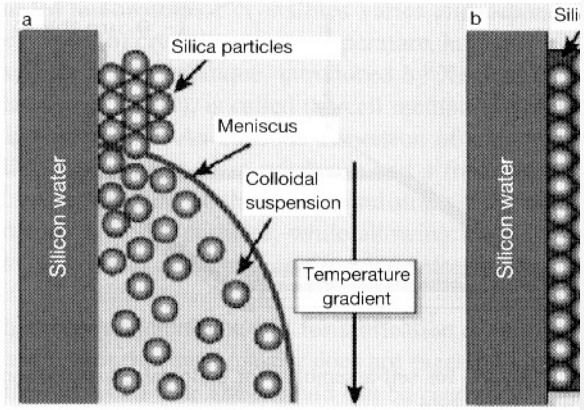

Figure 9.13. Vertical deposition method for crystallization of colloid
duced with permission from Joannopoulos, J. D., *Nature* **414,** 257–258 (2

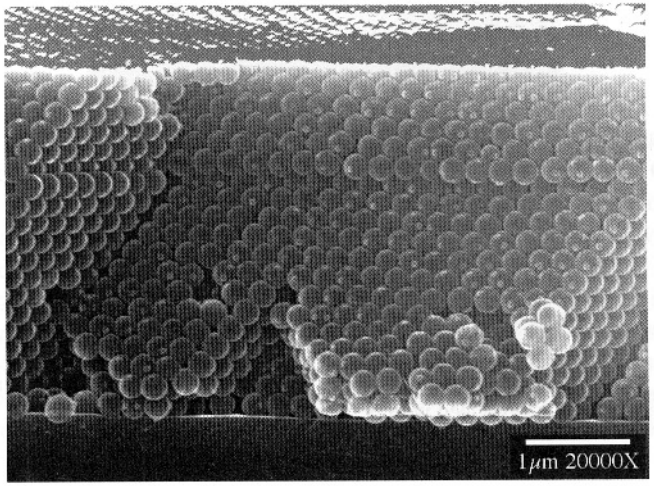

Figure 9.14. Scanning electron microscope (SEM) image of the polystyrene/air photonic crystal, prepared by the vertical deposition method.

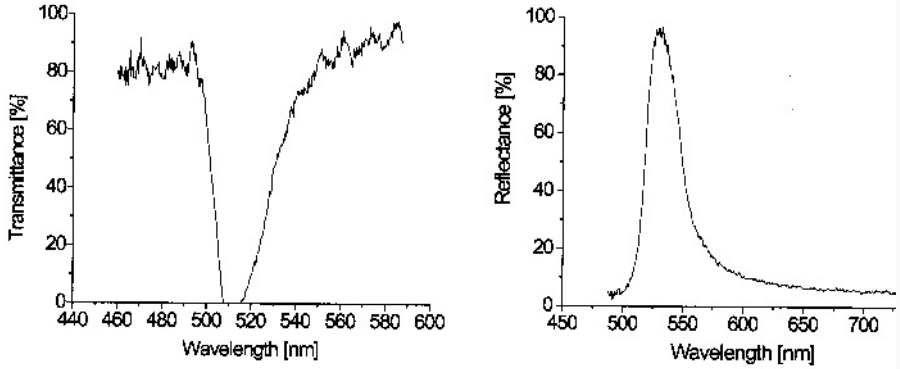

Figure 9.1. Typical transmission (a) and reflection (b) spectra of a photonic crystal pr
duced by close-packing of polystyrene spheres. The diameters of the polystyrene spheres a
220 nm for transmittance study and 230 nm for reflection measurement.

Huge interest in developing economic and reliable methods for PC mass fabrication

Examples of PCs II

See MRS Bull. 26 (Aug 2001)

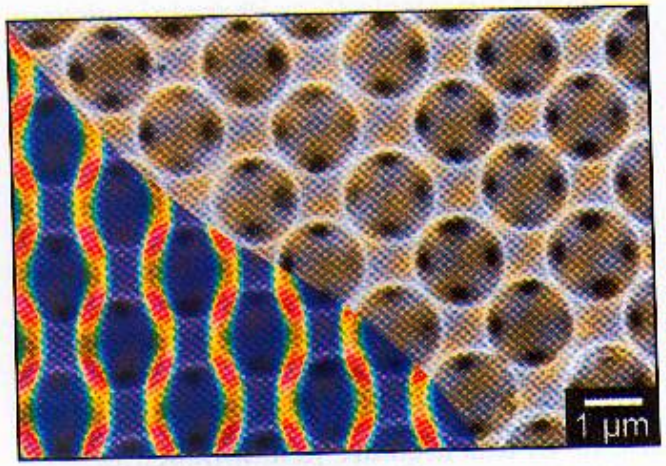

Figure 5. A scanning electron micrograph of a 3D photonic crystal. This structure was assembled by sedimentation of monodisperse colloidal silica on a template, thus forming an fcc structure. Subsequently, molten selenium, which has an index of refraction of 2.5 in the near-infrared and very low absorption, was imbibed into the interstitial space, and the silica was etched away to produce a high-dielectric-constant replica. (From Reference 9.)

Open question: 3D PC?

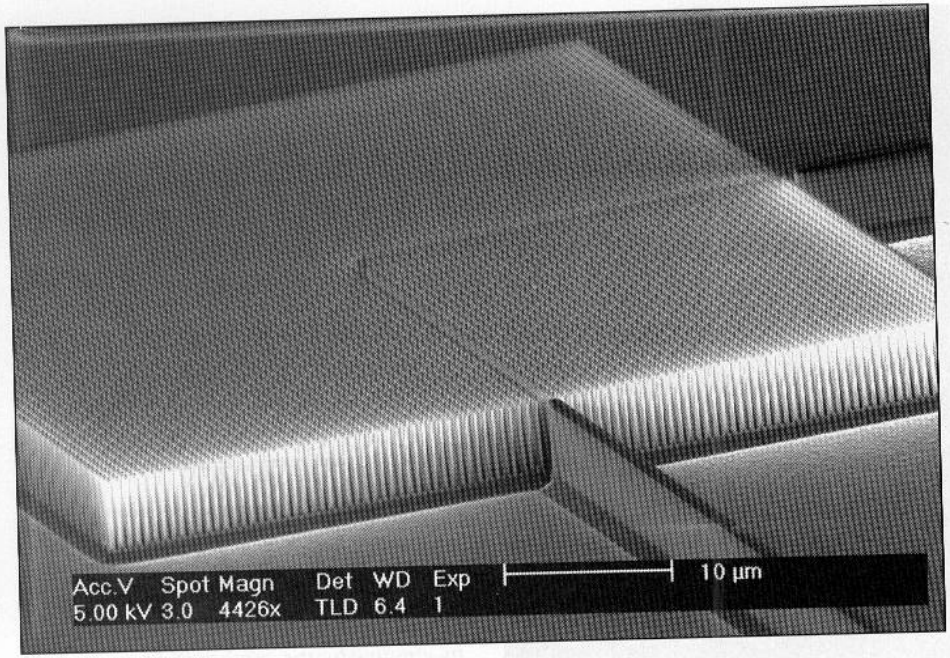

Figure 4. Scanning electron micrograph of a periodic array of silicon pillars fabricated using deep anisotropic etching. The silicon pillars are 205 nm in diameter and 5 µm tall. This structure possesses a bandgap of around 1.5 µm for transverse magnetic polarization. By removing an array of pillars, a waveguide bend may be fabricated. Input and output waveguides are integrated with the photonic crystal.

Huge interest in developing economic and reliable methods for integrating PCs and optoelectronics chips in advanced photonic devices

Conclusions

- ✓ Optics, optoelectronics and photonics have gained tremendous impulse from nanotechnology developments
- ✓ New diode lasers configuration available (or almost ready to the market) thanks to nanotechnology
- ✓ New and challenging applications (e.g., fluorescence markers in biology) envisioned for quantum dots
- ✓ The very old-known dependence of color on size reveals the role of metal nanoparticles in ruling the macroscopic optical behavior
- ✓ Innovative applications based on plasmonic nanodevices are on the way, with promised advantages in terms of miniaturization
- ✓ New possibilities exist to condition radiation in integrated optoelectronic devices thanks to photonic band gap crystals, which are also progressing thanks to technology advances

In summary, new technologies are bringing optics and photonics to unprecedented (and unexpected) levels of miniaturization